Monthly Notices
of the
ROYAL ASTRONOMICAL SOCIETY

MNRAS **472,** 3605–3623 (2017)
Advance Access publication 2017 August 29

doi:10.1093/mnras/stx2197

Observations of the galaxy cluster CIZA J2242.8+5301 with the Sardinia Radio Telescope

F. Loi,[1,2★] M. Murgia,[1] F. Govoni,[1] V. Vacca,[1] L. Feretti,[3] G. Giovannini,[3,4] E. Carretti,[1] F. Gastaldello,[5] M. Girardi,[6,7] F. Vazza,[3,8] R. Concu,[1] A. Melis,[1] R. Paladino,[3] S. Poppi,[1] G. Valente,[1,9] W. Boschin,[10,11,12] T. E. Clarke,[13] S. Colafrancesco,[14] T. Enßlin,[15] C. Ferrari,[16] F. de Gasperin,[17] L. Gregorini,[3] M. Johnston-Hollitt,[18,19] H. Junklewitz,[20] E. Orrù,[21] P. Parma,[3] R. Perley[22] and G. B. Taylor[23]

Affiliations are listed at the end of the paper

Accepted 2017 August 19. Received 2017 July 19; in original form 2017 May 22

ABSTRACT

We observed the galaxy cluster CIZA J2242.8+5301 with the Sardinia Radio Telescope to provide new constraints on its spectral properties at high frequency. We conducted observations in three frequency bands centred at 1.4, 6.6 and 19 GHz, resulting in beam resolutions of 14, 2.9 and 1 arcmin, respectively. These single-dish data were also combined with archival interferometric observations at 1.4 and 1.7 GHz. From the combined images, we measured a flux density of $S_{1.4\,\mathrm{GHz}} = (158.3 \pm 9.6)$ mJy for the central radio halo and $S_{1.4\,\mathrm{GHz}} = (126 \pm 8)$ and (11.7 ± 0.7) mJy for the northern and the southern relics, respectively. After the spectral modelling of the discrete sources, we measured at 6.6 GHz $S_{6.6\,\mathrm{GHz}} = (17.1 \pm 1.2)$ and (0.6 ± 0.3) mJy for the northern and southern relics, respectively. Assuming simple diffusive shock acceleration, we interpret measurements of the northern relic with a continuous injection model represented by a broken power law. This yields an injection spectral index $\alpha_{\mathrm{inj}} = 0.7 \pm 0.1$ and a Mach number $\mathrm{M} = 3.3 \pm 0.9$, consistent with recent X-ray estimates. Unlike other studies of the same object, no significant steepening of the relic radio emission is seen in data up to 8.35 GHz. By fitting the southern relic spectrum with a simple power law ($S_\nu \propto \nu^{-\alpha}$), we obtained a spectral index $\alpha \approx 1.9$ corresponding to a Mach number ($\mathrm{M} \approx 1.8$) in agreement with X-ray estimates. Finally, we evaluated the rotation measure of the northern relic at 6.6 GHz. These results provide new insights on the magnetic structure of the relic, but further observations are needed to clarify the nature of the observed Faraday rotation.

Key words: acceleration of particles – magnetic fields – galaxies: clusters: intracluster medium.

1 INTRODUCTION

In the standard scenario of hierarchical formation of the Universe large-scale structures form and grow through merger events involving dark matter dominated clumps-like galaxy clusters and galaxy groups. An example of these processes is gravitational-driven collisions between two sub-clusters of galaxies that end up with the formation of a more massive galaxy cluster. Such merging events represent the most spectacular and energetic processes since the big bang: they can release enormous amounts of energy in the intracluster medium (ICM), as much as $\gtrsim 10^{64}$ erg (Sarazin 2002).

In these environments, some galaxy clusters show diffuse synchrotron radio sources called radio haloes and relics (e.g. Feretti et al. 2012) found at the centre and at the periphery of the cluster, respectively. These sources are not associated with specific optical counterparts so they reveal the existence of a non-thermal component in the ICM made up of relativistic particles and magnetic fields spread over the cluster volume (e.g. Carilli & Taylor 2002). Radio haloes and relics have a typical size of ∼1 Mpc, low surface brightness (∼0.1–1 μJy arcsec^{-2} at 1.4 GHz) and are steep spectrum ($\alpha \gtrsim 1$). Relics are elongated arc-like sources usually oriented perpendicularly to the merger axis. While radio haloes are generally

★ E-mail: floi@oa-cagliari.inaf.it

observed to be unpolarized, there are a few cases where it has been possible to detect filaments of polarized emission (e.g. in A2255, Govoni et al. 2005; MACS J0717.5+3745, Bonafede et al. 2009; A523, Girardi et al. 2016). In contrast, relics exhibit high degrees of polarization (∼20–30 per cent) indicating that either the magnetic field in these sources is extremely ordered or it has been confined in a thin layer.

From the study of relics, one can make a step forward in understanding the physics of the ICM. Observations are consistent with the idea that relics trace shock waves occurring in merger events (Röttiger, Burns & Stone 1999), where shocks are identified as sharp discontinuities in the temperature and surface brightness distributions inferred from X-ray observations of galaxy clusters. In particular, Enßlin et al. (1998) proposed a diffusive shock acceleration mechanism (DSA, Drury 1983) to explain the re-acceleration of relativistic particles in relics. This mechanism does not put constraints on the nature of the injected relativistic particles. In this respect, recent observations are consistent with a scenario in which old electrons from nearby radio galaxies are re-accelerated through the DSA mechanism (e.g. Bonafede et al. 2014; van Weeren et al. 2017). However, a single acceleration of thermal electrons by shocks or a combination of acceleration and re-acceleration have been shown to produce quite similar results in a few specific cases (e.g. Kang & Ryu 2016). Radio observations of relics are also important to understand the evolution of large-scale magnetic fields. Shock waves amplify the fields to microGauss levels and align the magnetic field with the shock plane, as predicted by the aforementioned models and observed in terms of strong linearly polarized synchrotron emission associated with relics. Relics are usually observed at low frequencies with interferometers. However, due to the fact that interferometers are only sensitive to angular scales according to their minimum baseline length, single-dish telescopes are essential for the study of diffuse radio sources, especially at high frequencies (Emerson 2002). There are many examples of single-dish telescopes being used to investigate diffuse radio relics and haloes in literature (Farnsworth et al. 2013; Carretti et al. 2013; Kierdorf et al. 2017).

The Sardinia Radio Telescope[1] (SRT) is a new 64-m single-dish radio telescope, designed to operate in the frequency range 0.3–116 GHz, and currently working between 0.3 and 26 GHz (Bolli et al. 2015; Prandoni et al. 2017). It has recently been successful in spectro-polarimetric observations of galaxy clusters (Murgia et al. 2016). In this paper, we present the SRT observations of the galaxy cluster CIZA J2242.8+5301 (hereafter CJ2242). We observed CJ2242 with the SRT at 1.4, 6.6 and 19 GHz as part of the early science project SRT Multi-frequency observations of galaxy clusters (SMOG, project code S0001, PI: M. Murgia). The SMOG program consists of wide-band and wide-field spectral-polarimetric observations of a sample of galaxy clusters (Govoni et al. 2017). The aim of the project is to improve our knowledge of the non-thermal components (relativistic particles and magnetic fields) of the ICM on large scale and to shed light on the interplay between these components and the life cycles of cluster radio galaxies. This can be done through the comparison of SRT observations with radio observations at higher resolution and at different frequencies, and with observations in the millimetres, sub-millimetres, optical and X-ray.

The galaxy cluster CJ2242 has been included in the SMOG sample because it is an interesting case of system hosting a faint central halo and a double relic system (van Weeren et al. 2010) and it is located at a relatively low redshift of $z = 0.1921$ (Kocevski et al. 2007). The diffuse radio emission easily exceeds 15 arcmin, making single-dish observations with the SRT essential to measure the emission at all relevant angular scales.

The paper is organized as follows. In Section 2, we briefly illustrate the current knowledge about this cluster. In Section 3, we describe the details of the observations, the data reduction and the imaging of CJ2242 with the *L*-, *C*- and *K*-band receivers of the SRT. Total intensity images are shown in Section 4, where we include the combination of single-dish and interferometric maps at 1.4 GHz for the galaxy cluster. We also estimate the flux density of the diffuse and discrete sources and their spectral behaviour. In Section 5, we present the linearly polarized emission and the application of the rotation measure (RM) synthesis technique to *C*-band observations. Finally, the conclusions are presented in Section 6.

Throughout this paper, we assume a Λcold dark matter cosmology with $H_0 = 71\,\mathrm{km\,s^{-1}\,Mpc^{-1}}$, $\Omega_\mathrm{m} = 0.27$ and $\Omega_\Lambda = 0.73$. At the redshift of CJ2242, 1 arcmin corresponds to 189.9 kpc.

2 THE GALAXY CLUSTER CIZA J2242.8+5301

The galaxy cluster CJ2242 was discovered with X-rays by Kocevski et al. (2007) during a survey aiming at finding new cluster candidates at low Galactic latitudes ($l = 104.^\circ19$ and $b = -5.^\circ11$). They measured its redshift ($z = 0.1921$) and a luminosity ($L_\mathrm{X} = 4.0 \times 10^{44}\,\mathrm{ergs^{-1}}$) in the energy band 0.1−2.4 keV. Its disturbed elongated X-ray morphology suggested that this could be an example of cluster that underwent a merger event. van Weeren et al. (2010) confirmed this scenario using observations taken with the Westerbork Synthesis Radio Telescope (WSRT), the Giant Metrewave Radio Telescope (GMRT) and the Very Large Array (VLA). In their work, they presented the discovery of a faint central halo and a double relic system with a northern relic having a length of ∼2 Mpc, a width of ∼55 kpc and located 1.5 Mpc from the centre of the cluster. The radio morphology, together with the spectral index gradient of the northern relic towards the cluster centre, have been interpreted as signatures of acceleration and spectral aging of relativistic electrons due to the passage of a shock. Assuming the DSA model, they found a Mach number M ∼ 4.6 for the northern relic.

A reasonable scenario for this galaxy cluster is a collision in the plane of the sky (within 10°) between two sub-clusters with a mass ratio of 2:1 (confirmed by Okabe et al. 2015 using gravitational lensing) and an impact parameter $\lesssim$400 kpc. The core passage of the sub-clusters likely happened about 1 Gyr ago (van Weeren et al. 2011).

Association of the relics with shock fronts has been confirmed from *Suzaku* observations – Akamatsu & Kawahara (2013) measured a drop in temperature at the position of the northern relic, while the jump in the X-rays surface brightness was not detected, probably because of resolution limits. However, even with the highest spatial resolution X-ray data available (i.e. the *Chandra* data, Ogrean et al. 2014), the surface brightness discontinuity is still not detected. This aspect is very peculiar since at these high Mach numbers (M ∼ 2–4), the discontinuity should be remarkable, as is the case for El Gordo (Botteon et al. 2016) or A665 (Dasadia et al. 2016). Projection effects can be invoked, but the optical analysis by Dawson et al. (2015) points to the systems being in a nearly plane-of-the-sky merger configuration. Evidence for shock compression east of the southern relic has been observed with *XMM–Newton* by Ogrean et al. (2013). Recent estimates (Akamatsu et al. 2015)

[1] www.srt.inaf.it

of temperature drops from *Suzaku* observations suggest a Mach number M $\sim$ 2.7 and 1.7 for the northern and the southern relics, respectively.

The tension between Mach numbers for the northern relic inferred from radio and X-ray data was the first hint for physics beyond the DSA model. As a result, there were several attempts to find a consistent model for all observations of CJ2242 using numerical simulations (Donnert et al. 2017). However, new measurements of the radio flux injection index resulted in a Mach number M $\sim$ 2.9 (Stroe et al. 2014), in better agreement with the X-ray value inferred from the temperature jump detected by *Suzaku*. In recent years, CJ2242 has been observed over several radio frequency bands. In particular, Stroe et al. (2016) presented a study of the northern relic from 150 MHz to 30 GHz. They highlighted the steepening of the integrated spectrum beyond 2.5 GHz (from α = 0.90 to 1.77), claiming that the simple standard relic scenario could not hold for this galaxy cluster. Several models have been proposed to explain the steepening such as a time-variable magnetic field in the relic area (Donnert et al. 2016), or an additional population of fossil electrons that has broken out from the shock (Kang & Ryu 2016). However, interpretations based on the currently available high-frequency data (at 16 and 30 GHz) have to be taken with care because of their large uncertainties. These measurements are made from interferometric observations that could have lost a significant fraction of the total flux and can also be noticeably affected by the Sunyaev–Zel'dovich (SZ) effect (see Basu et al. 2016). These aspects have been taken into account in a recent work where the relic has been studied with single-dish observations conducted with the Effelsberg telescope (Kierdorf et al. 2016). They inferred a relic spectral index $\alpha = (0.90 \pm 0.04)$ between 150 MHz and 8.35 GHz and suggest that models describing the origin of relics have to include effects beyond the DSA mechanism that requires $\alpha > 1$, in order to physically model the relic. Similar findings have been reported for the cluster A2256 by Trasatti et al. (2015).

From this picture, it is clear how new, accurate high-frequency observations and estimates of the flux density of the northern relic are important to constrain the physical scenario of CJ2242.

3 OBSERVATIONS AND DATA REDUCTION

We observed the galaxy cluster CJ2242 at the SRT in three frequency ranges: *L*-band (1.3–1.8 GHz), *C*-band (6–7.2 GHz) and *K*-band (18–20 GHz). *L*- and *C*-band observations were centred at the J2000 coordinates RA $22^{\rm h}\,42^{\rm m}\,53\overset{\rm s}{.}1$ and Dec. $+53^\circ\,01'\,05''$, while *K*-band observations were centred on individual galaxies of the system. The details of the observations are reported in Table 1 (*L*- and *C*-band observations) and Table 2 (*K*-band observations).

We acquired spectral-polarimetric data in full-Stokes parameters with the SArdinia Roach2-based Digital Architecture for Radio Astronomy back end (SARDARA, Melis et al. in preparation) for the *L*- and *C*-band observations, while for the *K*-band observations only total intensity continuum observations were performed. For the data reduction and the imaging, we used the proprietary software package Single-dish Spectral-polarimetry Software (SCUBE, Murgia et al. 2016). In the following we describe, for each band, the observational set up and the procedure adopted for the data reduction and imaging.

L-band

We observed an area of $3^\circ \times 3^\circ$ with the entire 1.3–1.8 GHz band of the *L*-band receiver. We used the SARDARA back-end configuration with 1500 MHz bandwidth (the only option available to cover the entire 500 MHz band of the receiver) and 16 384 channels of 92 kHz each. The beam full width at half-maximum (FWHM) is about 14 arcmin at a frequency of 1.55 GHz. We performed several on-the-fly (OTF) maps in equatorial coordinates along the two orthogonal directions of RA and Dec. The telescope scanning speed was set to 6 arcmin $\rm s^{-1}$ and the scans were separated by 3.5 arcmin

Table 1. Details of the observations of the galaxy cluster CIZA J2242.8+5301 at the SRT in *L* and *C*-bands, acquired during the SMOG program. Columns report from left to right: the date, the receiver, the frequency range in GHz, the beam FWHM, the field of view (FoV), the number of on-the-fly (OTF) maps carried out, the calibrators used for the data reduction, the time spent on source (TOS).

Date	Receiver	Frequency (GHz)	FWHM (arcmin)	FoV	OTF scan axis	Calibrators	TOS (h)
2016 Jul 08	*L*-band	1.3–1.8	14	$3^\circ \times 3^\circ$	2×RA+1×Dec.	3C147	2.2
2016 Jul 12	*L*-band	1.3–1.8	14	$3^\circ \times 3^\circ$	1×RA+2×Dec.	3C147	2.2
2016 Feb 06	*C*-band	6.0–7.2	2.9	$1^\circ \times 1^\circ$	2×RA+2×Dec.	3C286, 3C84	2.3
2016 Jun 01	*C*-band	6.0–7.2	2.9	$1^\circ \times 1^\circ$	2×RA+1×Dec.	3C48, 3C84	2.5
2016 Jun 24	*C*-band	6.0–7.2	2.9	$30' \times 30'$	9×RA+9×Dec.	3C138, 3C48, 3C84	4.2
2016 Jun 26	*C*-band	6.0–7.2	2.9	$30' \times 30'$	9×RA+9×Dec.	3C138, 3C48, 3C84	5

Table 2. Details of the observations of some discrete sources, in the FoV of the galaxy cluster CIZA J2242.8+5301, at 19 GHz with an FWHM of 1 arcmin. Columns report from left to right: the source name, the source J2000 coordinates, the FoV of the scans, the number of the cross scans and the calibrators used for the data reduction.

Source	RA ($^{\rm h}\,^{\rm m}\,^{\rm s}$)	Dec. ($^\circ\,'\,''$)	FoV	Cross-scans	Calibrators
A	22 43 38.027	+53 09 19.47	$6' \times 6'$	20	3C147
B	22 42 44.666	+53 08 04.98	$6' \times 6'$	21	3C147
C	22 43 17.995	+53 07 19.84	$6' \times 6'$	22	3C147
D	22 42 48.004	+53 05 34.99	$6' \times 6'$	23	3C147
E	22 42 53.000	+53 04 50.00	$6' \times 6'$	11	3C147
G	22 42 51.338	+53 00 35.00	$6' \times 6'$	23	3C147
H	22 42 04.820	+52 59 34.39	$6' \times 6'$	11	3C147

to properly sample the SRT beam. We recorded the data stream by sampling at 10 spectra per second thereby producing individual samples separated by 36 arcsec along the scanning direction. For our purposes, we calibrated only the total intensity. Bandpass and flux density calibration were performed by observing 3C 147 assuming the flux density scale of Perley & Butler (2013). Those frequency windows affected by persistent radio-frequency interference (RFI) were flagged by hand. We also applied an automatic flagging procedure to excise the large amount of RFI randomly spread in frequency and time. The flagged data were then used to repeat the baseline subtraction, bandpass and flux density calibration. At these frequencies, the gain-elevation curve can be assumed to be flat and therefore we did not apply any correction. We subtracted the baseline of the OTF maps of CJ2242, scan by scan, by fitting 10 per cent of the data at the beginning and at the end of each scan. We projected the data in a regular three-dimensional grid with a spatial resolution of 180 arcsec pixel^{-1}. We then applied the automatic flag procedure on the target and we repeated the baseline subtraction and the projection. In total, we discarded about 30 per cent of the data. The total intensity image of CJ2242 is obtained by stacking all the calibrated OTF maps. In the combination, the individual image cubes were averaged and de-stripped by mixing their stationary wavelet transform (SWT) coefficients. Coefficients on a spatial scale below 2 pixels were omitted in order to improve the signal-to-noise ratio (S/N) without degrading the resolution. For further details, see Murgia et al. (2016).

C-band

We decided to make a shallow and a deep map, over a field of view (FoV) of $1^\circ \times 1^\circ$ and 30 arcmin × 30 arcmin, respectively. We used a 1.2 GHz bandwidth centred at 6.6 GHz. We acquired full-Stokes parameters in a bandwidth of 1500 MHz with the SARDARA back end, with 1024 channels of 1.46 MHz each. The beam FWHM at 6.6 GHz is 2.9 arcmin. We performed several OTF maps setting a spacing between the scans of 0.7 arcmin using a scan rate of 6 arcmin s^{-1} for the shallow map and 3 arcmin s^{-1} for the deep map. We acquired 33 spectra per second, therefore, on the sky, the spatial separation between individual samples along the scanning direction was 10.9 and 5.45 arcsec, for the shallow and the deep maps, respectively.

We calibrated the bandpass and the flux density by observing 3C 286, 3C 48 or 3C 138, depending on availability for each observation, assuming the flux density scale of Perley & Butler (2013). We removed RFI observed in a cold part of the sky and we repeated the calibration and RFI-flagging procedure until all the obvious RFI was removed. Then, we applied the gain-elevation curve correction to take into account the gain variations with elevation due to the telescope structure's gravitational stress change. For the polarization, we first corrected the delay between right and left polarizations of the receiver by using 3C 286, 3C 138 or 3C48. Next, we used 3C 84 to correct the instrumental polarization, and finally we corrected the absolute position of the polarization angle using 3C 286, 3C 138 or 3C48.

We subtracted the baseline of each scan of the OTF map of CJ2242. To take into account the presence of bright sources at the edge of the images, we decided to refine the baseline removal from each image cube using a mask. The mask has been obtained from the observation of CJ2242 at 1.4 GHz with the National Radio Astronomy Observatory (NRAO) VLA Sky Survey (NVSS, Condon et al. 1998): after a convolution of the map with the SRT beam we blanked all the pixels where the signal was larger than 1σ ($\sigma = 0.5$ mJy beam^{-1}), in order to keep just the noise regions. We proceeded by fitting the baseline of our images with a second-order polynomial, excluding the blanked regions in the mask. In this way, we could evaluate and subtract the noise more efficiently. We flagged the remaining RFI and then we repeated the baseline removal. The fraction of flagged data is ∼30 per cent. We projected the data in a regular three-dimensional grid with a spatial resolution of 42 arcsec pixel^{-1}. Afterwards, we stacked together all the RA–Dec. scans to obtain full-Stokes I, U and Q cubes. In the combination, the individual image cubes were averaged and de-stripped by mixing their SWT coefficients. Coefficients on a spatial scale below 2 pixels were omitted to improve the S/N without degrading the resolution. The polarized intensity P and the observed polarization angle Ψ were obtained from the U and Q maps by applying the relation $P = \sqrt{Q^2 + U^2}$ and $\Psi = 0.5 \cdot \arctan(U/Q)$. The polarization maps were corrected for the positive bias introduced when combining U and Q images (see appendix B in Killeen, Bicknell & Ekers 1986).

K-band

At 19 GHz, the diffuse emission of CJ2242 is very faint because of its steep spectrum. For instance, to detect the northern relic at 19 GHz with an S/N = 3, we would need to reach a sensitivity level of $\sigma = 0.1$ mJy beam^{-1} in the SRT images. Even with the SRT K-band multifeed, this would require more than 100 h of exposure time, too much to fit within the time allocated to the SMOG program.

Indeed, the K-band observations were aimed at characterizing the spectral behaviour of a few discrete sources embedded in the diffuse emission of the galaxy cluster CJ2242. In this way, we can have an accurate estimate of their flux densities at 6.6 GHz and disentangle the discrete and the diffuse emission of CJ2242 (see Section 4.3.2).

We performed total intensity continuum observations, using a total bandwidth of 2 GHz centred on 19 GHz, at which the FWHM is ∼1 arcmin. The coordinates of the cross-scans observations and other details are reported in Table 2.

After the baseline subtraction from each cross-scan, we calibrated the flux density with 3C 147 corrected for the atmosphere opacity and the gain variation with elevation. We used sky-dip observations to infer the opacity τ. The opacity during our observations was $\tau \simeq 0.02$. Finally, we projected the data in a regular two-dimensional grid with a cell size of 15 arcsec pixel^{-1} and we stacked all the cross-scans together to improve the S/N. We fitted the cross-scans with a two-dimensional Gaussian to derive the high-frequency flux density.

4 TOTAL INTENSITY RESULTS

4.1 *L*-band

4.1.1 Image

The results obtained from the L-band observations of CJ2242 are shown in Fig. 1 (top panel): contours start at 3σ with $\sigma = 20$ mJy beam^{-1} and colours refer to the NVSS image of the cluster. The central emission belongs to the galaxy cluster CJ2242. In the SRT image, we note two additional features. About 1° north of CJ2242 we see a diffuse arc-shaped structure which is likely due to a blending of discrete radio sources. North-east of CJ2242, at ∼10 Mpc from the cluster centre, we detect an extended 'L-shaped' structure which appears in the NVSS as a clustering of several point-like sources. In the bottom panel of Fig. 1, we show a zoomed figure including this extended structure and CJ2242.

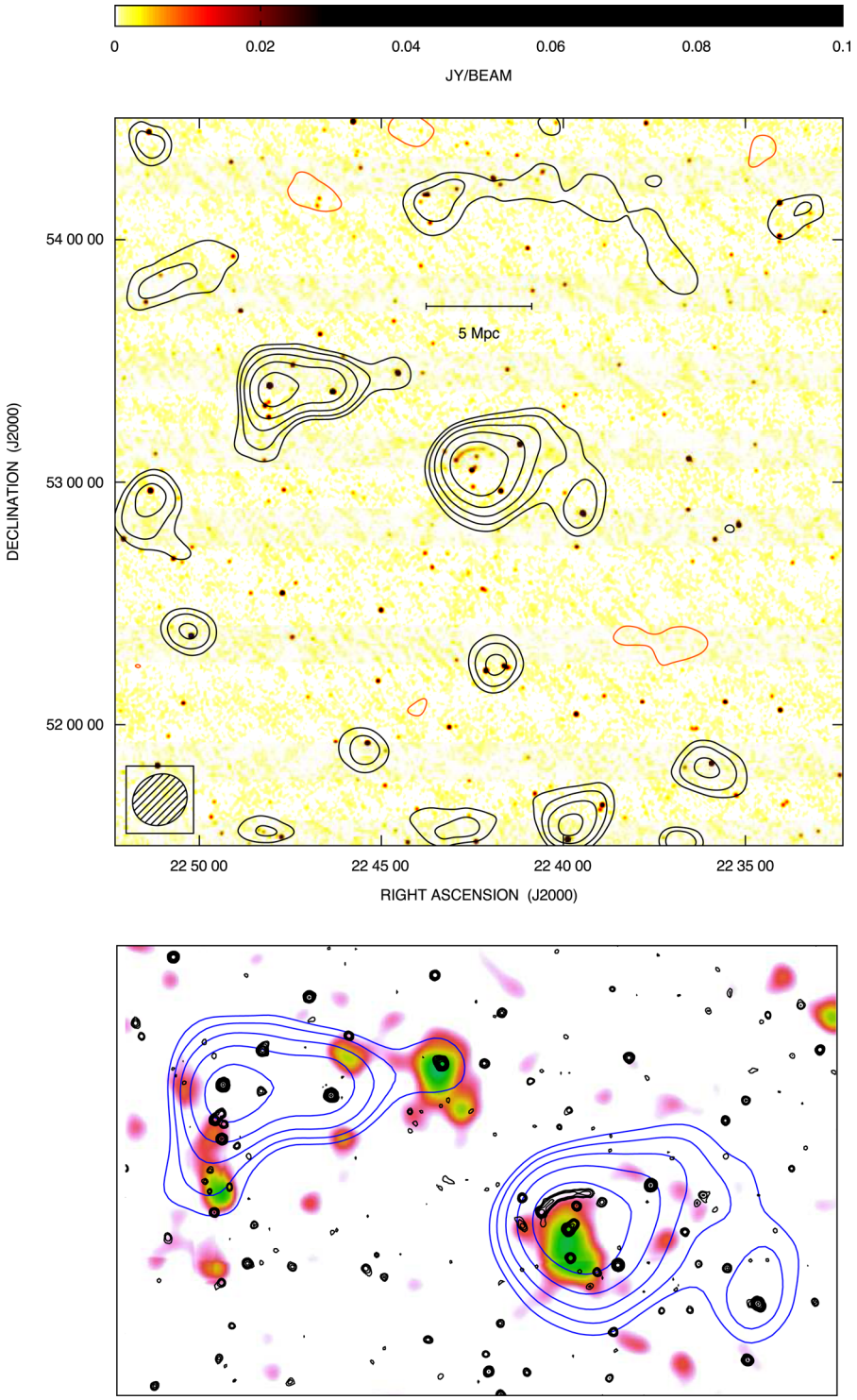

Figure 1. Top: NVSS image overlaid with the SRT total intensity contours of the galaxy cluster CIZA J2242.8+5301 obtained with the *L*-band receiver in the frequency range 1.3–1.8 GHz. The FoV of the image is $3^\circ \times 3^\circ$. The FWHM beam is 14 arcmin and is shown in bottom left corner. The noise level is 20 mJy beam^{-1}. Contours start at 3σ level and increase by a factor of $\sqrt{2}$ with negative contours (-3σ) drawn in orange. Bottom: a zoomed version including the L-shaped structure (see the text) and CJ2242 is shown. The SRT contours in blue and the NVSS contours in black are overlaid on the X-ray image taken from the RASS in the 0.1–2.4 keV band.

Colours refer to the X-ray image taken from the ROSAT All-Sky Survey (RASS, Trümper 1993) in the 0.1–2.4 keV band, corrected for the background, divided by the exposure map and smoothed with a Gaussian of $\sigma = 90$ arcsec. We overlaid the SRT contours in blue and those from NVSS in black. The SRT L-shaped structure seems to connect a few spots of X-ray emission: (1) on the west side, the closest to CJ2242, hosts at its centre an NVSS source; (2) another source, which is seen at the southern tip of the extended L-shaped structure, is somewhat fainter and overlaps in projection with several NVSS sources.

We wondered if the spatial coincidence between the radio and X-ray emission may possibly indicate the presence of one or more galaxy clusters, nearby to CJ2242. The association with high hardness ratios of sources in the ROSAT Bright Source Catalogue (Voges et al. 1999) and in the Faint Source Catalogue (FSC), coupled with the presence of an optical overdensity or SZ signal, is a good indication of the presence of a cluster (e.g. Ebeling, Mullis & Tully 2002; Planck Collaboration IV 2013). A bright source with a high hardness ratio, associated with optical overdensity, is the selection criterion of the CIZA catalogue itself (Kocevski et al. 2007, and references therein). This criteria can be extended to faint sources (Ebeling et al. 2013). The source closest to CJ2242 (labelled S1 in Section 4.2.1) is associated with the FSC source 1RXS J224504.3+532800, which has a hardness ratio of 0.93 ± 0.09. This is also confirmed by the second RASS source catalogue (2RXS, Boller et al. 2016) and the association with the source 2RXS J224454.9+532719 having a hardness ratio of 1.0 ± 0.1. See also Section 4.2.1.

4.1.2 *Combination of single-dish and interferometer data*

We combined our single-dish map together with interferometric maps from Stroe et al. (2013), available online,[2] taken with the WSRT at 1.4 and 1.7 GHz. Data were collected in the frequency ranges between 1.303–1.460 GHz and 1.642–1.780 GHz. The beam sizes of the WSRT images are 20.95 arcsec × 15.80 arcsec and 15.98 arcsec × 13.10 arcsec at 1.4 and 1.7 GHz, respectively. Their sensitivity is $\sigma = 40$ μJy beam^{-1} at 1.4 GHz and $\sigma = 30$ μJy beam^{-1} at 1.7 GHz.

As already mentioned in the Introduction, the angular extent of the diffuse emission in CJ2242 (radio halo and relics) exceeds 15 arcmin. The maximum structure that can be recovered by the WSRT at *L*-band, given the minimum baseline of $b_{\rm min} = 36$ m between the antennas of the array, is about 16 arcmin for a source at the zenith. As a result, a fraction of the flux density from the radio halo and the relics could have been missed by the WSRT, due to the lack of information in the inner portion of the (u, v)-plane. The single-dish SRT *L*-band image does not suffer from this limitation, since structures as large as the angular scale of the SRT image are retained (3°).

Therefore, we combined the SRT with the WSRT images to reconstruct the correct large-scale structure while preserving the angular resolution of the interferometric observations (see e.g. Stanimirovic et al. 1999).

We did this in the image plane using the SCUBE software package, in a similar way as the Astronomical Image Processing System (AIPS) task IMERG or the MIRIAD (Sault, Teuben & Wright 1995) task IMMERGE. In particular, we used the WSRT images which are already corrected for the primary beam attenuation. These images consist of a single pointing and are blanked outside a circular region of 55.3 and 45 arcmin, at 1.4 and 1.7 GHz, respectively. We extracted two smaller sub-bands from the full SRT bandwidth (1.3–1.8 GHz), centred at the exact central frequencies and with the same bandwidths as the WSRT data. We cropped the two SRT images produced from these sub-bands in the same way as the WSRT images to contain the same region of the sky. After that, we transformed the single-dish and the interferometric images to combine them in Fourier space. The diameter of the SRT, 64 m, is larger than the minimum baseline of the WSRT, therefore in the Fourier plane there is a region of overlap in which both images share the same power spectral density. This annulus in the Fourier space is used to cross-check the calibration of the two images and to calculate a scaling factor that we then applied to the single-dish data. In order to account for the different resolution of the two instruments, we deconvolved the images, by dividing both of them by the Fourier transforms of the corresponding Gaussian beams, before calculating the scaling factor.

Due to the superior S/N, the scaling factor was calculated at 1.7 GHz. The required adjustment resulted in a scaling-up factor for the SRT image of 1.23 that we also applied to the SRT 1.4 GHz image. After this scaling, the two power spectra were merged using a weighted sum of the Fourier transforms. For the single-dish observations, data weights are set to 0 for all wavenumbers larger than the outer ring of the annulus, while they are set to 1 in the inner portion of the Fourier plane. In the annulus, the weights linearly vary from 0 to 1. The interferometric data are weighted in a similar way but with swapped values for the weights.

The combined Fourier spectrum was then tapered by multiplying by the transform of the interferometer beam. The combined image, obtained by the antitransform, has the same angular resolution of the original WSRT image and includes the large-scale structures detected by the SRT.

Results are shown in Fig. 2: at left, we present the WSRT maps at 1.4 GHz (top) and 1.7 GHz (bottom) and on the right, we show the WSRT and SRT combined maps. Contours start at 3σ level. Thanks to the combination, we can recover the flux density associated with the diffuse sources of the galaxy cluster CJ2242, revealing a greater extension of the central radio halo, especially at 1.4 GHz. At 1.7 GHz, we do not see a significant enhancement of the radio halo emission. This could be consistent with the fact that typically these sources have a steep spectrum ($\alpha = 1.3$) such that at higher frequencies the associated flux could be lower than the rms of the map. Assuming the same size at the two frequencies, the mean surface brightness at 1.7 GHz should be $\langle {\rm I}_{1.7\,{\rm GHz}} \rangle = \langle {\rm I}_{1.4\,{\rm GHz}} \rangle \times 0.485$, a factor that takes into account the different beam areas of the two instruments. At 1.4 GHz, $\langle {\rm I}_{1.4\,{\rm GHz}} \rangle \sim 3.8 \times \sigma_{1.4\,{\rm GHz}}$ that implies $\langle {\rm I}_{1.7\,{\rm GHz}} \rangle \sim 0.074$ mJy beam^{-1}. Thus, in order to detect the radio halo at 1.7 GHz, we would need a noise level of $\sigma = 25$ μJy beam^{-1}, lower than the rms of the image.

4.1.3 *Flux density measurements of diffuse sources*

We measured the flux density of the diffuse emission of the galaxy cluster CJ2242 at 1.4 GHz using the combination of SRT and WSRT data.

As we do not observe radio halo emission in the WSRT 1.7 GHz image of Fig. 2 at the 3σ level we used this image to blank the strong sources in the field of CJ2242 from the 1.4 GHz images. We ended up with an image where the discrete sources and the relics are blanked as shown by blue contours in Fig. 3.

In this image, black represents the emission above the 3σ level of the combined map at 1.4 GHz. We assumed that this is the extent of the radio halo and that the relics are located inside the red contours. We defined the northern relic region by taking all those pixels inside the same area considered by Stroe et al. (2016) in fig. A1 with a flux density greater than 5σ, excluding obvious discrete sources. The southern relic emission is fainter than that of the northern relic. Thus, to isolate the southern relic from the radio halo, we used a stronger limit in flux by drawing a 8σ-level contour around the relic. We used the black area outside the blue contours (equivalent

[2] http://vizier.cfa.harvard.edu/viz-bin/VizieR?-source=J/A+A/555/A110

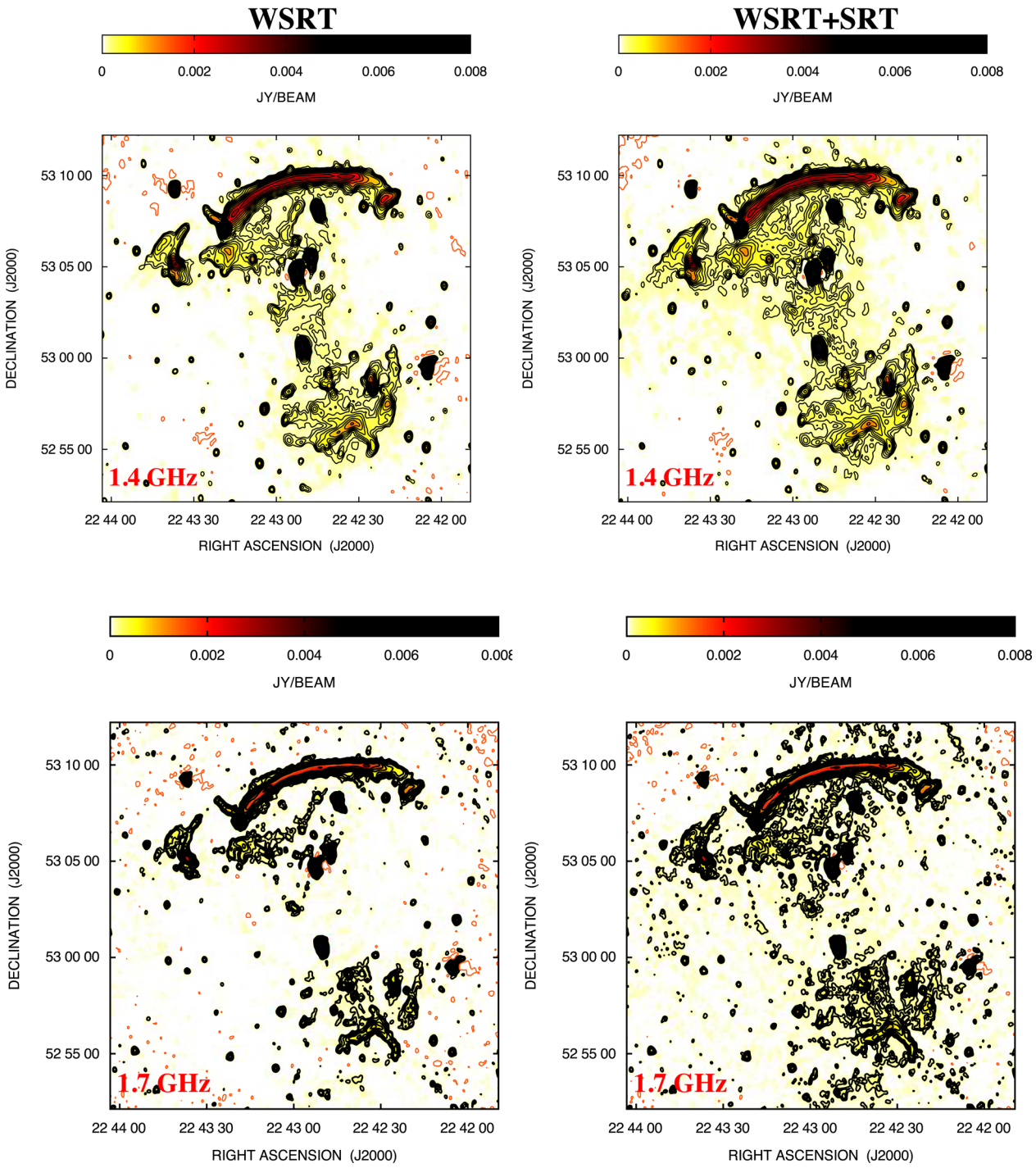

Figure 2. Results of the single-dish interferometer combination: on the left, we show the WSRT maps at 1.4 GHz (top) and 1.7 GHz (bottom) taken from Stroe et al. (2013) and on the right, the WSRT and SRT combination maps. Contours start at 3σ level, where $\sigma = 40$ μJy beam^{-1} at 1.4 GHz and $\sigma = 30$ μJy beam^{-1} at 1.7 GHz, and increase by a factor of $\sqrt{2}$. Negative contours (-3σ) are drawn in orange. The beam sizes of the images are 20.95 arcsec × 15.80 arcsec at 1.4 GHz and 15.98 arcsec × 13.10 arcsec at 1.7 GHz.

to ∼451 times the beam area) to evaluate a mean surface brightness of the radio halo. Then, we multiplied this value with the total area (equivalent to ∼869 times the beam area), as we assume that the halo extends even in the relic regions and that of the discrete sources.

We found that the radio halo hosted by CJ2242 has a total flux density of $S_{1.4\,\mathrm{GHz}}^{\mathrm{SRT+WSRT}} = (158.3 \pm 9.6)$ mJy. We noticed that if we measure with the same procedure the radio halo flux from the WSRT 1.4 GHz image, we find $S_{1.4\,\mathrm{GHz}}^{\mathrm{WSRT}} = (115 \pm 7)$ mJy. In our estimates, we included statistical and systematic (6 per cent of the flux to include calibration uncertainties) errors. The northern relic has a total flux density of $S_{1.4\,\mathrm{GHz}}^{\mathrm{WSRT}} = (121 \pm 7)$ mJy and $S_{1.4\,\mathrm{GHz}}^{\mathrm{WSRT+SRT}} = (126 \pm 8)$ mJy as calculated from the interferometric and combined maps, respectively. Here, we have subtracted the contribution of the extended radio halo in order to take into account only the flux density of the northern relic. Finally, we found that the southern relic has a flux density $S_{1.4\,\mathrm{GHz}}^{\mathrm{WSRT+SRT}} = (11.7 \pm 0.7)$ mJy,

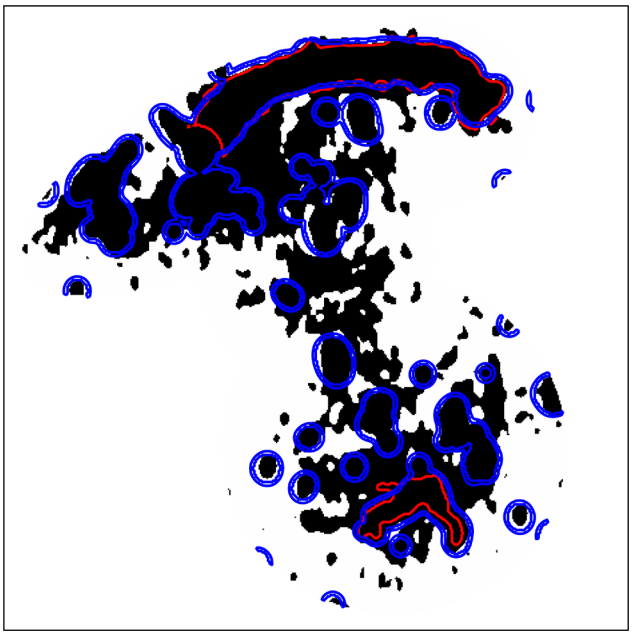

Figure 3. This image shows the area we considered to measure the flux of the diffuse sources hosted by CIZA J2242.8+5301: red contours are drawn around the relic areas, while black colour corresponds to the radio halo emission. Blue contour indicates that strong sources that we do not considered in the estimate of the halo mean surface brightness.

a value consistent, within errors, with that calculated from the interferometric map, $S^{\rm WSRT}_{1.4\,\rm GHz} = (11.0 \pm 0.7)$ mJy.

For the radio halo, we find an enhancement of the flux density of about ∼38 per cent when we combine single-dish and interferometric images, whereas for the relics, we obtain no significant differences. This demonstrates how the interferometer has poor sensitivity to extended and diffuse emission, while it performs better with narrow structures such as the northern relic.

The statistical properties of radio haloes in galaxy cluster are important in order to understand the nature of these sources. Thanks to our measurements, we can now compare the properties of CJ2242 with other clusters that host radio haloes. In Fig. 4, we plot the 1.4 GHz power of the radio halo versus the X-ray luminosity between 0.1 and 2.4 keV (top) and the 1.4 GHz power of the radio halo versus its largest linear size (bottom) measured at the same frequency. Filled dots are observed clusters taken from the literature. We added to the compilation by Feretti et al. (2012) new radio haloes in merging galaxy clusters revealed through pointed interferometric observations at ≃1.4 GHz (Govoni et al. 2012; van Weeren et al. 2012; Giovannini et al. 2013; Martinez Aviles et al. 2016; Shakouri et al. 2016; Parekh et al. 2017). A red triangle marks the cluster CJ2242, one of the largest radio haloes and one of the brightest.

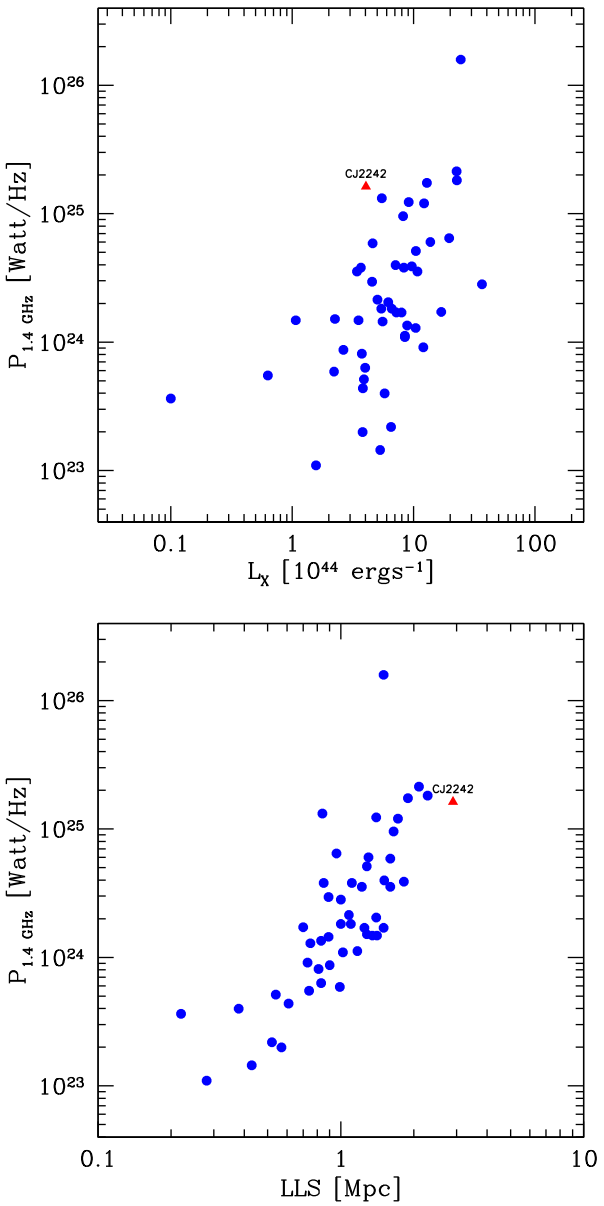

Figure 4. Radio halo power at 1.4 GHz versus the cluster X-ray luminosity in the 0.1–2.4 keV band (top) and versus the largest linear size of the radio halo measured at 1.4 GHz (bottom). Full dots are observed clusters taken from the literature. We added to the compilation by Feretti et al. (2012) new radio haloes in merging galaxy clusters revealed through pointed interferometric observations at ≃1.4 GHz (Govoni et al. 2012; van Weeren et al. 2012; Giovannini et al. 2013; Martinez Aviles et al. 2016; Shakouri, Johnston-Hollitt & Pratt 2016; Parekh et al. 2017). A red triangle marks the cluster CJ2242.

4.2 Shallow *C*-band

4.2.1 Image

In Fig. 5 (bottom), we show the resulting total intensity contour map in the frequency range between 6 and 7.2 GHz over a region of $1^\circ \times 1^\circ$. We reached a noise level of $\sigma = 1$ mJy beam^{-1} with a beam size of 2.9 arcmin × 2.9 arcmin. The radio contours at 6.6 GHz are overlaid on the same X-ray image as Fig. 1, taken from the RASS in the 0.1–2.4 keV band. The central cluster is bright both in the X-ray and radio band and we detected the diffuse radio emission associated with CJ2242.

Among the external sources, marked with a letter in the image, the most interesting is S1. As already pointed out in Section 4.1.1, the X-ray emission has the right hardness ratio to be classified as a galaxy cluster candidate. We show in Fig. 5 (top), contours of the 323 MHz GMRT image of Stroe et al. (2013). These contours are drawn starting from 2 mJy beam^{-1} and increase by a factor of 2. Thanks to the higher resolution of the GMRT, we can appreciate the head–tail morphology of the source which is further indication of the presence of a dense external medium similar to what is

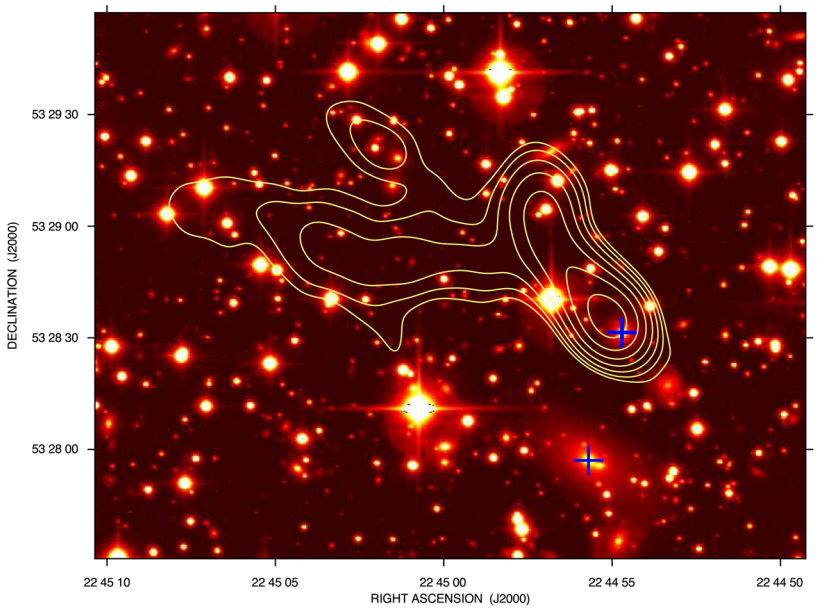

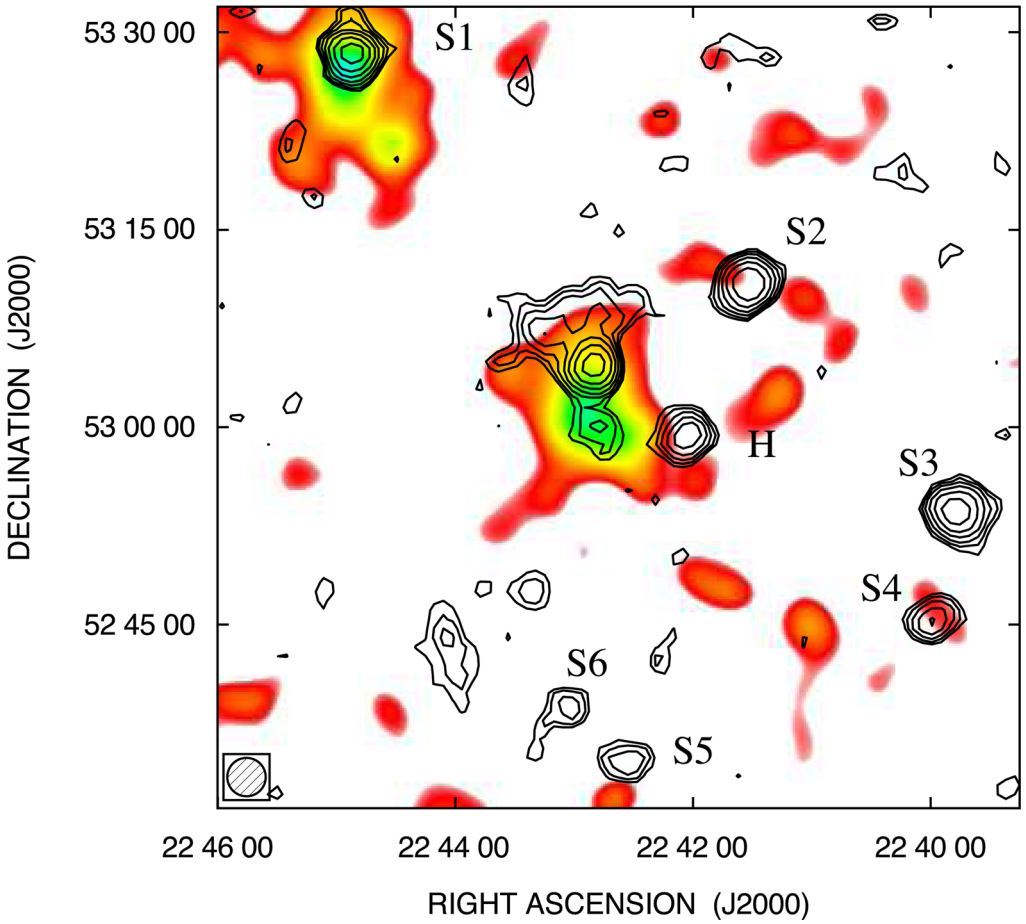

Figure 5. Top: CFHT optical image of S1 with the two optical galaxies indicated by the crosses and contours from the 323 MHz GMRT image that start at 2 mJy beam^{-1} and increase by a factor of 2. Bottom: shallow SRT total intensity contour image of the galaxy cluster CIZA J2242.8+5301 at 6.6 GHz overlaid on the X-ray image taken from the RASS in the 0.1–2.4 keV band. The SRT image has been obtained from the spectral average of the data in the frequency range 6−7.2 GHz. The FoV is $1^\circ \times 1^\circ$. The FWHM beam is 2.9 arcmin and is shown in bottom left corner. Contours start at 3σ level, with $\sigma = 1$ mJy beam^{-1}, and increase by a factor of $\sqrt{2}$.

Table 3. Flux measurements of the sources marked in Fig. 5 obtained from the NVSS 1.4 GHz (Condon et al. 1998) and the SRT 6.6 GHz images (this work).

Label	Name	$S^{\rm mJy}_{1.4\,\rm GHz}$	$S^{\rm mJy}_{6.6\,\rm GHz}$	α
S1	NVSS J224455+532840	133 ± 8	28 ± 2	1.00 ± 0.09
S2	87GB 223927.9+525526	138 ± 8	26 ± 2	1.08 ± 0.09
S3	4C +52.50	182 ± 11	26 ± 2	1.3 ± 0.1
S4	NVSS J224001+524538	35 ± 2	9 ± 1	0.9 ± 0.1
S5	NVSS J224234+523506	32 ± 2	6 ± 1	1.1 ± 0.2
S6	NVSS J224258+523912	11 ± 1	5 ± 1	0.5 ± 0.2
H	NVSS J224205+525931	99.6 ± 0.6	14 ± 2	1.3 ± 0.2

typically found in galaxy clusters. The radio contours are overlaid on an optical Canada–France–Hawaii Telescope (CFHT) image,[3] where two blue crosses indicate the position of two optical galaxies: 2MASX J22445464+5328318, at less than 0.2 arcmin from S1, and 2MASX J22445565+5327578, at less than 0.7 arcmin. The galaxies have a *K*-band magnitude of $M = (13.5 \pm 0.1)$ and (12.67 ± 0.06) mag, respectively, already corrected for extinction (see appendix in Schlafly & Finkbeiner 2011). By using the *K*-band magnitude–redshift relations of Inskip et al. (2002), we found that these galaxies have a redshift $z \sim 0.1$–0.2, similar to CJ2242. We obtained a similar result ($z \sim 0.15$–0.2) when considering the *K*-band magnitude–redshift relation for brightest cluster galaxies (see fig. 5 in Stott et al. 2008).

Even if at the moment, there are only two optical galaxies identified in the vicinity of S1, this fact, together with its X-ray properties and the fact that S1 is a head–tail radio source, corroborates the hypothesis of S1 as a cluster candidate.

4.2.2 *Flux density measurements of discrete sources*

In Table 3, we give the flux density of the sources identified in the field and marked with a letter in Fig. 5, measured from the NVSS 1.4 GHz and the SRT 6.6 GHz images. We also calculated the spectral index α of the sources assuming for the flux density S_ν, a power-law behaviour with the frequency ν,

$$S_\nu = S_0 \left(\frac{\nu}{\nu_0}\right)^{-\alpha}. \quad (1)$$

For source S1, we found $\alpha = 1.00 \pm 0.09$ which is typical for head–tail sources as pointed out in the previous section.

4.3 Deep *C*-band

4.3.1 *Image*

In Fig. 6, we show the total intensity map resulting from all the observations at 6.6 GHz in an FoV of 30 arcmin × 30 arcmin centred on the cluster centre. In this image, we reached a noise level of $\sigma = 0.5$ mJy beam^{-1}. Here, the two relics are clearly detected.

4.3.2 *Discrete sources modelling*

We characterize the spectral behaviour of the discrete sources, at less than 15 arcmin from the cluster centre, by using the following multifrequency high-resolution images of the galaxies:

(i) from the NRAO archive, we retrieved observations from the program AV312 presented by van Weeren et al. (2010), which used the VLA in C configuration at 4835 and 4885 MHz. We calibrated data following standard procedures using the AIPS software package;

(ii) we used GMRT 323, 608 MHz and WSRT 1714, 2272 MHz images from Stroe et al. (2013) available online;[4]

(iii) we included in our sample, the Westerbork Northern Sky Survey (WENSS) at 325 MHz (Rengelink et al. 1997) and the NVSS at 1400 MHz (Condon et al. 1998) maps;

(iv) we also added the SRT 19 GHz observations reported in Table 2.

We considered the nine sources marked in Fig. 7, whose flux is mixed with the diffuse sources at the SRT resolution. In this image, colours represent the SRT total intensity image at 6.6 GHz, and contours are from the VLA 4.8 GHz contours at 5σ level. We measured the flux density of each point-like source using a two-dimensional Gaussian fit, while for the extended sources, we integrated the radio brightness down to the first isophote above the noise level.

In Table 4, we present the values obtained including a systematic error of 10 per cent of the source flux, to take into account the different calibration scales of the images. Fig. 7 shows the resulting spectra: in each panel, the corresponding source is indicated in the bottom left corner with red dots indicating SRT 19 GHz measurements listed in Table 4 together with other measurements shown by black dots. Spectra are modelled by using the software SYNAGE (Murgia et al. 1999). The continuous blue line is the result of the fit using parameters as reported in the top right corner of each panel.

The spectra of A, B, C, D, E, G, and I are well described by a continuous injection (CI) model (Pacholczyk 1970), where the sources are continuously and constantly replenished with new relativistic electrons by the active galactic nucleus and the power-law spectrum breaks due to energy losses caused by the synchrotron radiation itself and inverse Compton scattering with the cosmic microwave background (CMB) photons. The CI model includes three free parameters: the injection spectral index, $\alpha_{\rm inj}$, that characterizes the spectrum below the break frequency, $\nu_{\rm b}$, and the normalization. Above $\nu_{\rm b}$, the high-frequency spectral index is:

$$\alpha_{\rm h} = \alpha_{\rm inj} + 0.5 \quad (2)$$

From these parameters, we can evaluate the synchrotron age of the source $t_{\rm s}$, i.e. the time elapsed since the start of the injection:

$$t_{\rm s} = 1590 \frac{B^{0.5}}{(B^2 + B^2_{\rm IC})[(1+z)\nu_{\rm b}]^{0.5}}\ {\rm Myr} \quad (3)$$

where B is the magnetic field in μG of the source and $B_{\rm IC}$ is the equivalent magnetic field due to the inverse Compton of the CMB that depends on redshift $B_{\rm IC} = 3.25(1+z)^2$ μG. The break frequency is in GHz. We calculated the synchrotron age by adopting the equipartition value $B_{\rm min}$ for the magnetic field strength (see eq. A.12 in Murgia et al. 2012). Since this value depends on the source volume we derived $B_{\rm min}$ and hence the age only for the extended sources B, C, D, E and G. The results of the spectral modelling and the source ages are listed in Table 5.

Source A: it is point-like, the spectrum is fitted by a CI model with $\alpha_{\rm inj} = 0.5$, and $\nu_{\rm b} = 1.4$ GHz. The observed spectrum includes SRT measurements at 19 GHz.

Source B: the spectrum for this source is described by a CI model, with $\alpha_{\rm inj} = 0.43$ and $\nu_{\rm b} = 0.6$ GHz. It is a small double of 164 kpc in

[3] http://www.cadc-ccda.hia-iha.nrc-cnrc.gc.ca/en/search/

[4] http://vizier.cfa.harvard.edu/viz-bin/VizieR?-source=J/A+A/555/A110

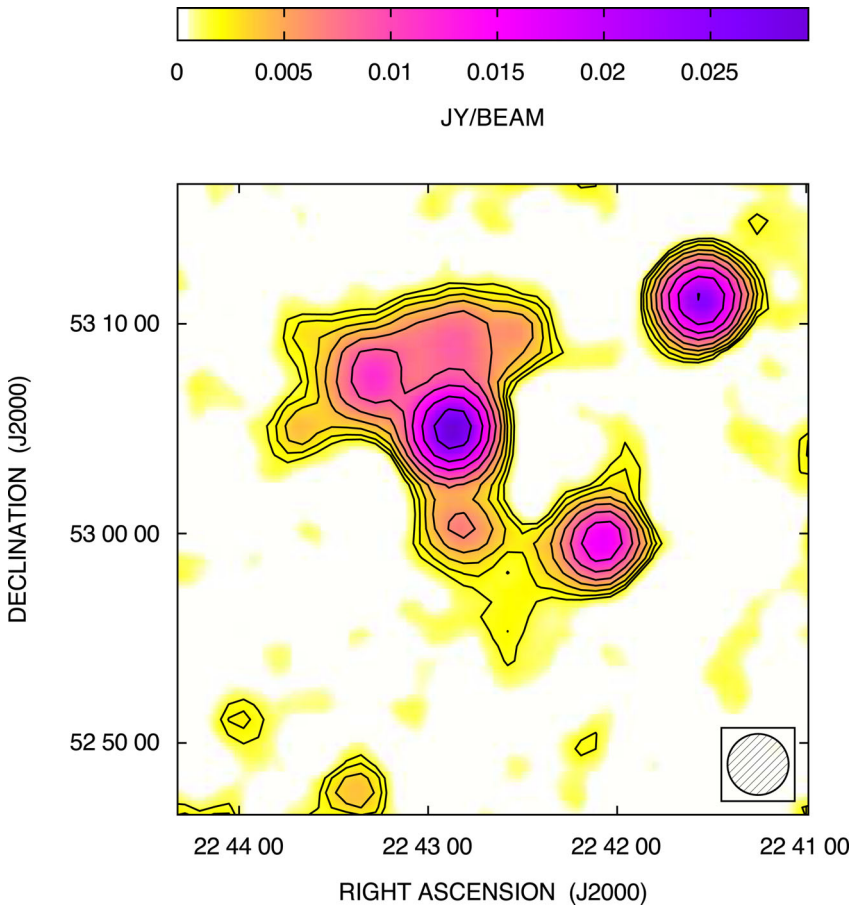

Figure 6. Deep SRT total intensity image of the galaxy cluster CIZA J2242.8+5301 obtained from the spectral average over the frequency range 6−7.2 GHz. The FoV of the image is 30 arcmin × 30 arcmin. The FWHM beam is 2.9 arcmin and is shown in bottom right corner. The noise level is 0.5 mJy beam^{-1}. Contours start at 3σ level and increase by a factor of $\sqrt{2}$.

size. Assuming a cylindrical volume, we calculated an equipartition magnetic field of $B_{\rm min} \approx 8.1$ μG, and we deduce an age of $t_{\rm s} = 76$ Myr.

Source C: this is a narrow-angle tail source, seen in projection over the northern relic. The tail, which has a linear size of 146 kpc, extends towards the north-east. We calculate for this source an age of $t_{\rm s} = 70$ Myr.

Source D: this source is seen in projection close to the cluster centre, and is slightly extended at the resolution of the VLA 4.8 GHz image. The spectrum is well fit by a CI model. We estimate an age of 46 Myr.

Source E: this source is located in projection close to the cluster centre. Its morphology shows two bright lobes and two faint tails extending in the N-S direction. The spectrum is fitted by a CI model with $\nu_{\rm b}$ =22 GHz and has an estimated age of $t_{\rm s} = 45$ Myr.

Source F: this source is located at the eastern tip of the northern relic. For this source, we added the flux density measurements we derived from the 150 MHz TIFR GMRT Sky Survey (TGSS[5]) (Intema et al. 2017) and the WSRT 153 MHz (Stroe et al. 2013) images: $S_{150\,\rm MHz} = (65 \pm 6)$ mJy and $S_{153\,\rm MHz} = (67 \pm 2)$ mJy. The radio spectrum shows a sharp high-frequency exponential cut-off that cannot be explained by the smooth steepening of the CI model. This source seems to be an example of a dying source where the central black hole of the galaxy has stopped its activity (Murgia et al. 2011). Following these authors, we fitted the radio spectrum using the CI$_{\rm OFF}$ model. This model assumes that the CI phase is followed by a remnant (or dying) phase during which the radio jets are switched off. In the absence of the injection of new electrons, the sources spectrum develops an exponential high-frequency cut-off. By fitting the CI$_{\rm OFF}$ model, we derived the break frequency which gives the total source age, and $t_{\rm OFF}/t_{\rm s}$, which gives the relative duration of the dying phase. We found a total source age of 149 Myr. The source has been in the active phase for 45 Myr and in the dying phase for 104 Myr. The morphology is relaxed, as expected for dying sources, but a weak point-like core is present. This weak core seems however to be disconnected from the fading lobes as no jets are visible.

Source F could be a potential source of seed electrons for the northern relic (e.g. Bonafede et al. 2014; van Weeren et al. 2017). By looking at the top right panel of Fig. 2, we see that the source is close to an arc-like feature which appears to be a secondary shock or a possible extension of the northern relic, although a discontinuity between these two structures is present.

Source G: this is a narrow-angle tail with a linear size of 174 kpc. The spectrum is well described by a CI model, with $\nu_{\rm b} \approx 0.9$ GHz. The source age is 166 Myr from which we deduced an advancing speed for the galaxy of $1000 \pm 400 \times \frac{1}{\sin(i)}$ km s^{-1}, where i is the inclination of the source with respect to the line of sight.

[5] http://tgssadr.strw.leidenuniv.nl/doku.php

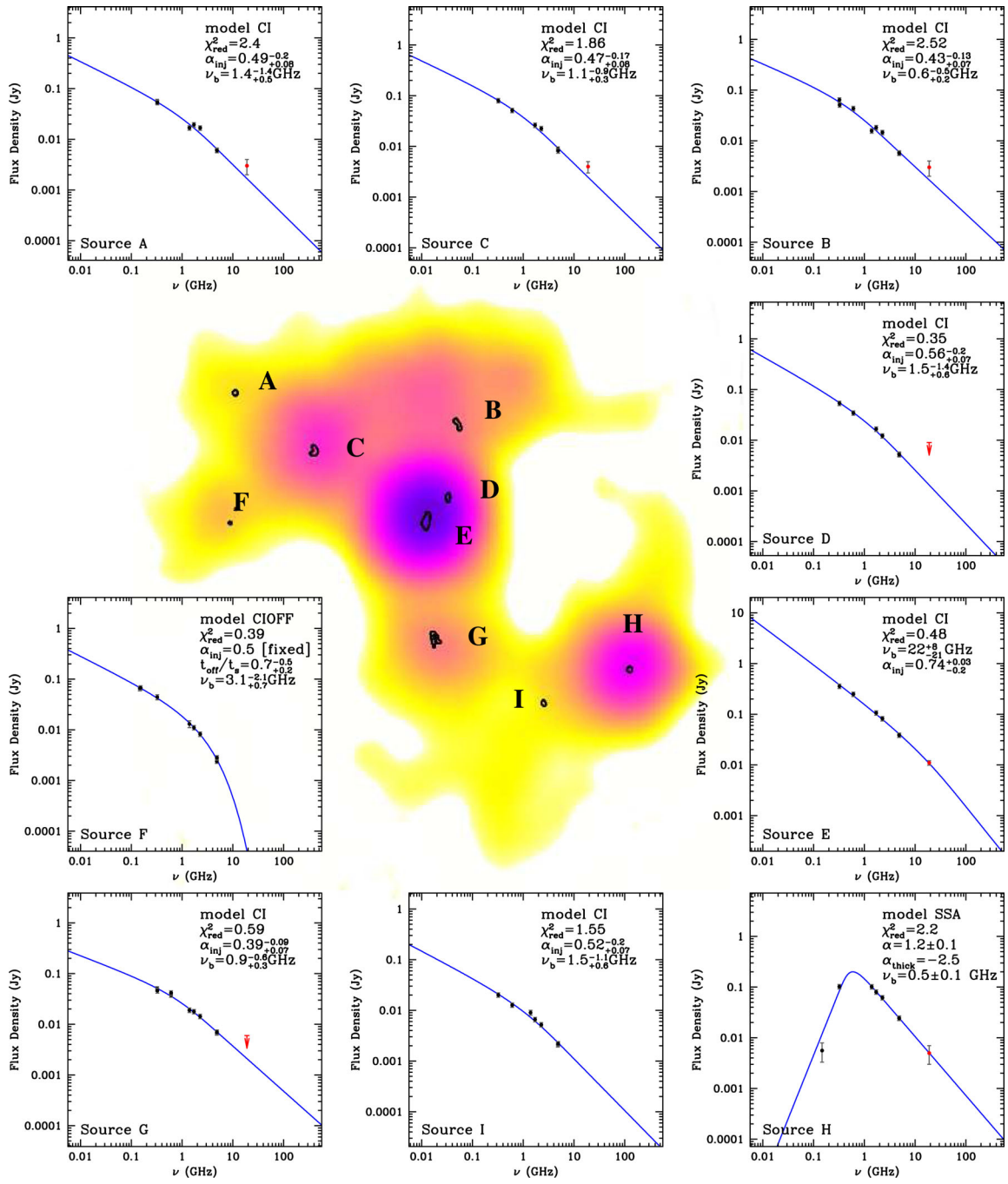

Figure 7. The image is the deep 6.6 GHz SRT total intensity map of the galaxy cluster CIZA J2242.8+5301 with VLA contours at 5σ level (σ = 0.03 mJy beam^{-1}). Each plot around the image refers to the spectrum of the discrete source specified in the bottom left corner. Black points are the flux density measurements from GMRT, WSRT, WENSS, NVSS and VLA images, while red points indicate the 19 GHz SRT measurements (see the text for details). The continuous blue line is the result of the fit whose parameters are reported in the top right corner of each panel.

Source H: for this source, we added the flux density measurement derived from the 150 MHz TGSS image: $S_{150\,\mathrm{MHz}} = (5.6 \pm 2.3)$ mJy. This source exhibits a spectral turnover at low frequencies that could be due to synchrotron self-absorption (SSA). In the optically thick part of the spectrum, we fixed the spectral index to $\alpha_{\mathrm{thick}} = -2.5$, while we modelled the optically thin regime using a power law. The source is unresolved and could be intrinsically a compact steep-spectrum source where the break frequency is below the SSA peak: $\nu_{\mathrm{b}} << \nu_{\mathrm{SSA}}$. For this reason, the observed spectral index in the optically thin part of the spectrum is interpreted as $\alpha = \alpha_{\mathrm{inj}} + 0.5$.

Source I: the spectrum of this source is well fit by a CI model with the break at 1.5 GHz and $\alpha_{\mathrm{inj}} \approx 0.5$. The source is point-like.

From the fitted spectra, we derived the flux density of the sources at $\nu = 6.6$ GHz and report these in the last column of Table 4.

4.3.3 *Flux density measurements of diffuse sources*

As mentioned in the Introduction, single-dish telescopes can be used to accurately infer the size and flux density of diffuse sources. They are not affected by the missing zero-spacing problem that

Table 4. Flux density measurements obtained from the following maps: GMRT 323 MHz (Stroe et al. 2013), WENSS 325 MHz (Rengelink et al. 1997), GMRT 608 MHz (Stroe et al. 2013), NVSS 1400 MHz (Condon et al. 1998), WSRT 1714 MHz (Stroe et al. 2013), WSRT 2272 MHz (Stroe et al. 2013), VLA 4835 MHz and 4885 MHz (van Weeren et al. 2010) and SRT 19 GHz (this work). We report the expected flux density of each source at 6.6 GHz in the last column.

Source	$S^{\rm mJy}_{323\ \rm MHz}$	$S^{\rm mJy}_{325\ \rm MHz}$	$S^{\rm mJy}_{608\ \rm MHz}$	$S^{\rm mJy}_{1.4\ \rm GHz}$	$S^{\rm mJy}_{1.7\ \rm GHz}$	$S^{\rm mJy}_{2.2\ \rm GHz}$	$S^{\rm mJy}_{4.835\ \rm GHz}$	$S^{\rm mJy}_{4.885\ \rm GHz}$	$S^{\rm mJy}_{19\ \rm GHz}$	$[S^{\rm mJy}_{6.6\ \rm GHz}]^{\rm exp}$
A	56 ± 6	53 ± 5	–	17 ± 2	19 ± 2	17 ± 2	6.1 ± 0.6	6.0 ± 0.6	3 ± 1	4.8
B	64 ± 6	51 ± 5	43 ± 4	16 ± 2	18 ± 2	15 ± 2	5.8 ± 0.6	5.7 ± 0.6	3 ± 1	4.6
C	80 ± 8	–	51 ± 5	–	26 ± 3	22 ± 2	8.9 ± 0.9	8.2 ± 0.8	4 ± 1	6.9
D	54 ± 5	–	35 ± 3	–	17 ± 2	12 ± 1	5.4 ± 0.5	5.2 ± 0.5	6 ± 3	4.0
E	357 ± 36	–	248 ± 25	–	106 ± 11	82 ± 8	39 ± 4	39 ± 4	11 ± 1	31.0
F	–	44 ± 5	–	13 ± 2	11 ± 1	8.2 ± 0.8	2.4 ± 0.2	2.8 ± 0.3	–	1.4
G	50 ± 5	46 ± 5	38 ± 4	42 ± 4	19 ± 2	18 ± 2	14 ± 1	6.8 ± 0.7	3 ± 2	5.4
H	102 ± 10	–	–	102 ± 10	80 ± 8	62 ± 6	24 ± 2	24 ± 2	5 ± 2	17.4
I	20 ± 2	–	13 ± 1	9 ± 1	6.6 ± 0.7	5.2 ± 0.5	2.1 ± 0.2	2.2 ± 0.2	–	1.4

Table 5. Results of the spectral modelling and source ages.

Source	Model	$\alpha_{\rm inj}$	$\nu_{\rm b}$ (GHz)	$B_{\rm min}$ (μG)	$t_{\rm s}$ (Myr)
A	CI	0.5 ± 0.1	1.4 ± 1.0	–	–
B	CI	0.4 ± 0.1	0.6 ± 0.4	8.1	76 ± 36
C	CI	0.5 ± 0.1	1.1 ± 0.6	6.9	70 ± 24
D	CI	0.6 ± 0.1	1.5 ± 1.0	8.4	46 ± 22
E	CI	0.7 ± 0.1	22 ± 14	10.2	45 ± 16
F	$\rm CI_{OFF}$	0.5	3 ± 1	1.4	149 ± 60
G	CI	0.4 ± 0.1	0.9 ± 0.5	3.6	166 ± 58
H	SSA+PL	0.7 ± 0.1	< 0.54	–	–
I	CI	0.5 ± 0.1	1.5 ± 0.6	–	–

plagues radio interferometers, especially at high frequency where the primary beam is usually smaller than the cluster size in the local Universe. Unfortunately, the typical beam of single-dish telescopes is far larger than the beam synthesized by the interferometer, so it is difficult to distinguish between diffuse and discrete sources.

Thanks to the spectral modelling of the discrete sources from the previous section, we have a firm prediction of their flux densities at 6.6 GHz (see last column of Table 4).

We modelled these sources with Dirac delta functions normalized to the expected fluxes. We then convolved these functions with the SRT beam and finally we subtracted the resulting image from our SRT 6.6 GHz image.

Fig. 8 shows in grey scale and magenta contours, the total intensity deep image on the right and, on the left, the image with the sources subtracted, where we expect to observe the contribution of diffuse emission only. The noise is $\sigma = 0.5$ mJy beam^{-1}. Both images show yellow contours of the combined image at 1.4 GHz presented in Fig. 2. At the 3σ level, the northern emission seems to extend beyond the strong galaxy C covering a total extension of $\sim$2.9 Mpc and a width of $\sim$800 kpc. However, the extra component in the north-east direction could be either due to a real extension of the northern relic or to the residual flux from source F (see notes on Section 4.3.2). For these reasons, and to be consistent with the other measurements (see fig. A1 of Stroe et al. 2016), we evaluated the northern relic flux density inside the ellipse drawn with a dashed line in Fig. 8. At the 5σ level (a cut consistent with that of Kierdorf et al. 2016), we found $S_{6.6\,\rm GHz} = (17.1 \pm 1.2)$ mJy.

From Fig. 8, we can also give an estimate of the flux of the southern relic at 6.6 GHz. We measured a flux density of $S_{6.6\ \rm GHz} = (0.6 \pm 0.3)$ mJy at the 3σ level.

4.4 Northern and southern relics

Our results regarding the flux of the northern relic are reported in Table 6 together with flux density measurements at different frequencies taken from literature up to 8.4 GHz. We included the value we inferred from the WENSS 327 MHz image after the subtraction of sources A, B and C, with the flux densities expected from our models at 327 MHz.

In Fig. 9, we plot the values of Table 6. The red points represent our measurement obtained with the SRT observations. We fit the spectrum of the northern relic with a CI model (blue line). This model takes into account the presence of relativistic particles injected at early stages of the shock passage that have lost their energy resulting in a break in the spectrum. From the fit, we obtain a value of the injection spectral index $\alpha_{\rm inj}$. This value is related to the spectral index $\alpha_{\rm h}$ as already shown in equation (2).

From the fit, we know that the spectrum breaks at $\nu_{\rm b} = 1.8^{+0.6}_{-1.5}$ GHz and that $\alpha_{\rm inj} = (0.7 \pm 0.1)$, in agreement with van Weeren et al. (2010). In the high-frequency region of the spectrum ($\nu >> \nu_{\rm b}$), where radiative losses are balanced by the injection of new particles, the resulting spectral index is $\alpha_{\rm h} = (1.2 \pm 0.1)$. By applying the simple DSA model formula:

$$M = \sqrt{\frac{\alpha_{\rm h} + 1}{\alpha_{\rm h} - 1}} \tag{4}$$

we inferred a Mach number $\rm M = (3.3 \pm 0.9)$ in agreement within the errors of the value $\rm M = 2.7^{+0.7}_{-0.4}$ presented in Akamatsu et al. (2015). However, we noticed that there is not yet a clearly detected jump in the X-ray surface brightness as expected at these Mach numbers (Donnert et al. 2017, see discussion in Section 2).

In the frequency range probed by our observations no significant evidence of steepening in the radio spectrum is found beyond that predicted by the CI model. From our analysis based on a wide-frequency range (from 150 MHz to 8.35 GHz), we can exclude the steepening found by Stroe et al. (2016) beyond 2.5 GHz. Moreover, we find that the CI model is consistent with the data. Thus, the physics of the northern relic of CJ2242 does not seem to require models beyond the standard DSA mechanism, although only new accurate measurements at frequencies higher than 10 GHz can definitively exclude alternative scenarios.

It should be noted that Stroe et al. (2016) presented interferometric measurements at 16 and 30 GHz taken with the Arcminute Microkelvin Imager and with the Combined Array for Research in Millimeter-wave Astronomy. These measurements are represented as open dots in Fig. 9. We do not include them in our fit procedure, since these measurements are made with interferometers that could

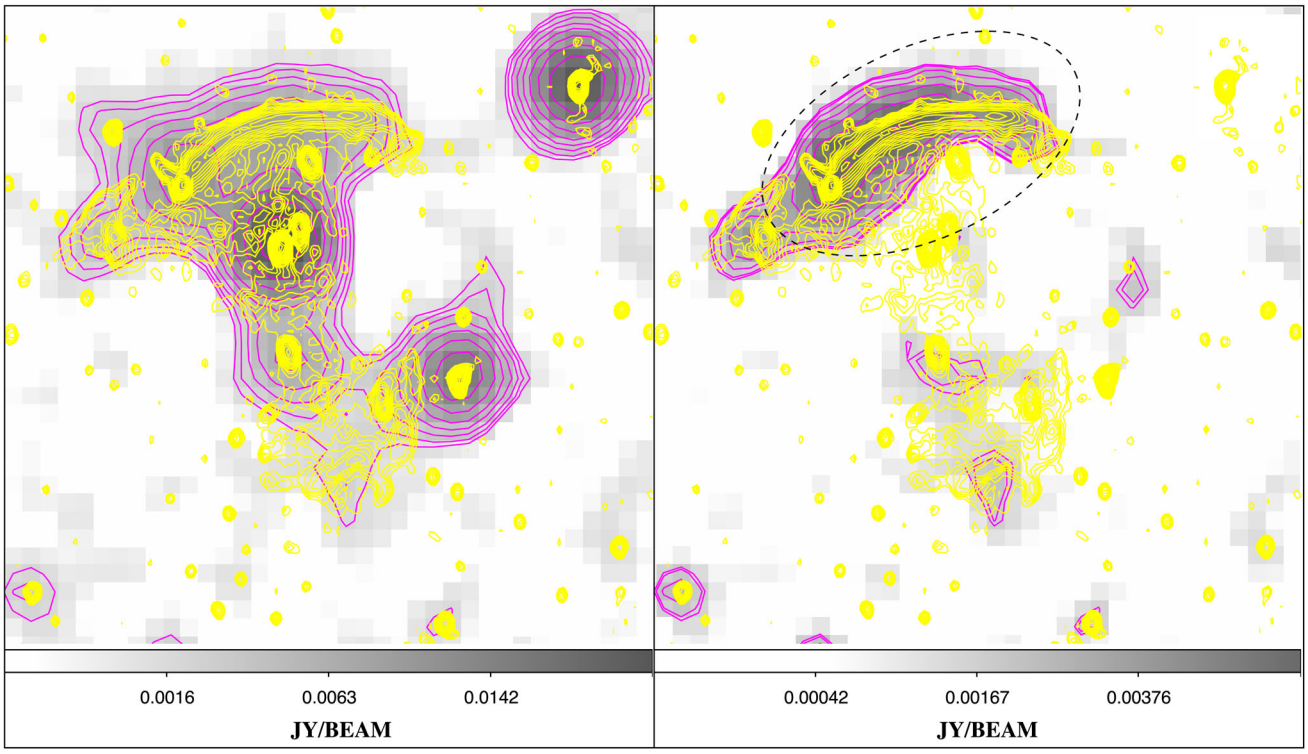

Figure 8. Left: the original SRT image at 6−7.2 GHz (colour-scale + magenta contours) overlaid with the higher resolution WSRT+SRT 1.4 GHz contours (yellow). Right: the residual 6−7.2 GHz image of the diffuse emission after the subtraction of modelled discrete sources (see the text for details). Again the WSRT+SRT 1.4 GHz contours are overlaid in yellow.

Table 6. Flux density measurements of the northern relic of CIZA J2242.8+5301.

ν (GHz)	S_ν (mJy)	Reference
0.15	780.4 ± 80	Stroe et al. (2016)
0.325	315.7 ± 32.4	Stroe et al. (2016)
0.327	446 ± 21	This work, WENSS image
0.61	222.3 ± 22.4	Stroe et al. (2016)
1.2	125.7 ± 12.6	Stroe et al. (2016)
1.4	126 ± 8	This work, SRT image
1.7	91.2 ± 9.2	Stroe et al. (2016)
2.25	61 ± 3.6	Stroe et al. (2016)
2.3	54.3 ± 5.6	Stroe et al. (2016)
4.85	32 ± 8	Kierdorf et al. (2016)
6.6	17.1 ± 1.2	This work, SRT image
8.35	17 ± 5	Kierdorf et al. (2016)

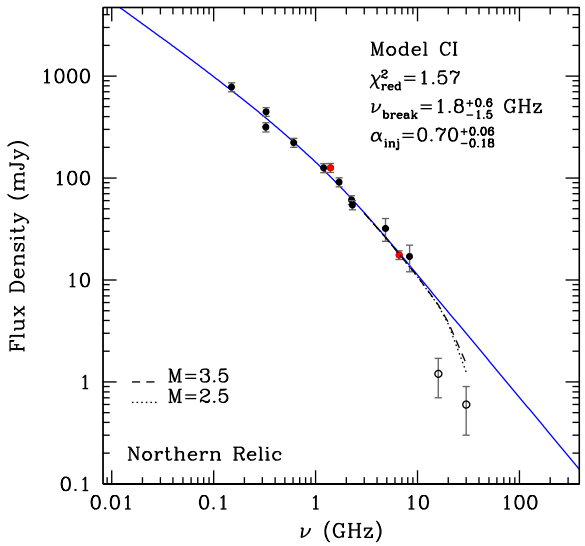

Figure 9. Total flux measurements of the northern relic at different frequencies from Table 6. Red points are the new measurements from this paper obtained with the SRT observations. The blue line represents the CI model fit whose parameters are shown in the top right corner of the image. Dot and dashed lines have been drawn to show the flux density decrement due to the SZ effect as predicted for the northern relic of CJ2242 by Basu et al. (2016) assuming M = 2.5 and 3.5, respectively.

have lost a significant fraction of the flux density from the extended structure. None the less, we compare them with the best fit of the CI model taking into account the SZ decrement. Extrapolating the CI model at frequencies higher than 10 GHz, we show as a dot and dashed lines in Fig. 9 the SZ decrement as expected by Basu et al. (2016) for this relic assuming a Mach number of M = 2.5 and 3.5, respectively.

As we can see the decrement is negligible, or at least within the flux calibration uncertainties until ∼16 GHz. Above this frequency, the SZ decrement is increasingly significant, but not enough to explain the measurements at 16 and 30 GHz.

The observed gap could be due to a missing flux problem, as previously mentioned, or it could be real. In the latter case, a modification from the basic CI model is required. Donnert et al. (2016) showed that a non-uniform magnetic field in the region of the relic could explain the flux densities measured at 16 and 30 GHz. Future single-dish observations at frequencies higher than 10 GHz, which could be obtained with the SRT seven-feed *K*-band receiver, could help to shed light on the claimed high-frequency steepening.

It should be noted that the break frequency of the CI model corresponds to the spectral break of the oldest electron population injected only if the particles are confined within the volume of the radio source, and the radio spectrum is extracted from a region that encloses the entire emitting region. In this case, we can think at the CI model as the sum of all electron populations from the youngest to the oldest ones. Below the break frequency (where radiative losses are negligible), particles accumulate and the source luminosity grows linearly with time. Above the break frequency, a steady state is reached and the high-frequency spectrum stays unchanged since radiative losses are compensated by the freshly injected particles (Kardashev 1962; Pacholczyk 1970). If the magnetic field has been constant in time and uniform in space inside the radio source we can use equation (3) to estimate the time since the start of the injection, provided that we know the magnetic field strength. This assumption was used to estimate the ages of the discrete sources embedded in the diffuse emission in Section 4.3.2. However, this basic scenario needs to be modified if the confinement time τ_c of the particles inside the source is finite which is likely the case for relics. We can make the oversimplified assumption that the shocked region consists of a slab of enhanced magnetic field strength of width $l_{\rm relic}$. Particles are accelerated in the outer rim of the slab at the edge of the upstream region by the shock wave and then they flow and age backwards in the downstream region. As the particles exit the slab, their radio emission rapidly disappears even at low frequencies due to the drop in the magnetic field strength. Indeed, the confinement time is related to the relic width by $\tau_c = l_{\rm relic}/v_d$, where v_d is the downstream velocity. Note that a similar argument has been advocated in Carilli et al. (1991) to explain the spectra of the hotspots in Cygnus-A, where particles are injected (or re-accelerated) at the termination shock inside the hotspots and then they backflow into the radio lobes. By definition, the age of the oldest electrons still present in the relic region and that produce the spectral break seen in the CI spectrum should be exactly τ_c. The magnetic field strength inside the relic is not known, however, from equation (3), it can be shown that the maximum age allowed for the electrons is $t_{\rm max} = 62$ Myr, which is obtained for $B = B_{\rm IC}/\sqrt{3} \simeq 2.7$ μG. We highlight that this value is in agreement with the minimum energy field strength of $B_{\rm min} = 2.4$ μG estimated by Kierdorf et al. (2016). Therefore, by assuming a the relic width $l_{\rm relic} \simeq 200$ kpc (Stroe et al. 2016), we can derive a lower limit for the downstream velocity of $v_d > 3145$ km s^{-1} or M > 3. We note that this lower limit is high but still compatible, within the measurement errors, with the Mach number derived both from the X-rays and from the DSA model (see equation 4). It is reasonable to assume (see Section 5.2) that the ambient magnetic field in the proximity of the relic is of the order of 1 μG. Indeed, the average magnetic field strength inside the relic region would be amplified by a factor $\gtrsim$2. This represents the average magnetic field strength in the compression region, while outside we suppose that the magnetic field drops to the background level. The particles that flow in the de-compressed region disappear rapidly, even at low frequencies, because of the drop in the spectrum normalization due to the weaker magnetic field. We stress that, according to this simple scenario, the break frequency of the CI model is not related to the time necessary to the shock to propagate from the cluster centre to the observed position (∼0.5 Gyr), but rather it refers to the much shorter confinement time of the electrons inside the shocked region. Therefore, we cannot infer the total age of the relic (that however, we can assume to be larger than τ_c), since the very first injected particles are not contributing anymore to the current observable radio spectrum. We underline that in this calculation, we assumed that the magnetic field strength profile is described by a simple step function. A more detailed treatment of this issue is beyond the scope of this work; we refer to Donnert et al. (2016) for a more sophisticated modelling. These authors consider much smoother profiles for the magnetic fields after the shock (resulting from their assumption of a small-scale dynamo in the downstream region), which results in a curvature for the high-frequency spectrum more pronounced with respect to that of the CI model.

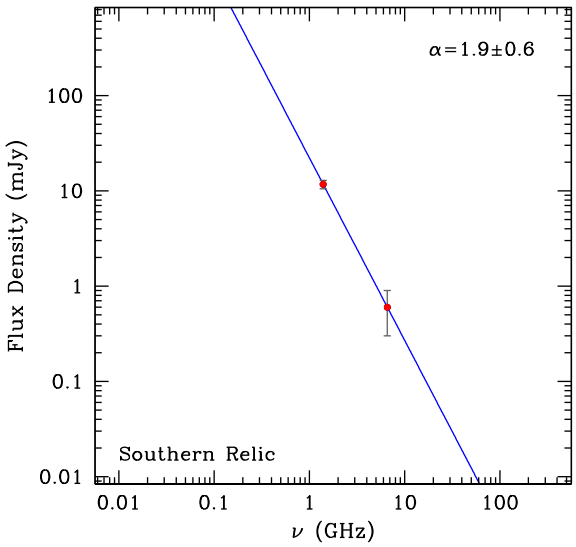

Figure 10. Total flux measurements of the southern relic obtained with the SRT observations.

In any case, it is important to point out that a steep-spectrum power-law behaviour is expected only if the confinement time is so long that the break frequency of the oldest population present in the relic region shifts below the lower end of the observed window. Attempts to fit the spectrum with a single power law have been presented in Kierdorf et al. (2016). They found for CJ2242 $\alpha = 0.90 \pm 0.04$ which is intermediate between $\alpha_{\rm inj}$ and α_h in our fit. However, this value of spectral index leads to problematic results, since the Mach number expected by the DSA model diverges. We therefore opt for the CI fit, under the assumption that the spectral curvature is real, since the missing flux problem is negligible below 1 GHz. This is confirmed by the finding that the flux density of the relic before and after the single-dish–interferometric combination is roughly the same at *L*-band.

Concerning the southern relic: we fitted our estimates of the flux density at 1.4 and 6.6 GHz with a simple power law as shown in Fig. 10. Because only two experimental points were available the fit of the CI model is not applicable. The southern relic has a spectral index $\alpha \simeq 1.9$ corresponding to a Mach number of M $\simeq$ 1.8. Even in this case, the value is in agreement with that found by Akamatsu et al. (2015, $M = 1.7^{+0.4}_{-0.3}$).

After the submission of our paper ,we became aware of the work of Hoang et al. (2017) where these authors present Low-Frequency Array observations between 115.5 and 179 MHz and a study of the diffuse sources of CJ2242. Assuming the DSA model and by evaluating the injection spectral index in the upstream region, they find Mach numbers for the southern and the northern relics in agreement with the ones obtained from X-rays by Akamatsu et al. (2015) and consistent with our results.

5 POLARIZED INTENSITY RESULTS

5.1 *C*-band

Fig. 11 shows, on the left, the SRT 6.6 GHz linearly polarized intensity image of CJ2242 in colours as detected from the deep observations (FoV = 30 arcmin × 30 arcmin). Contours refer to the total intensity image (Fig. 6) and vectors indicate the electric-field polarization. In this image, the noise level is $\sigma = 0.35$ mJy beam^{-1}.

We detect the polarized emission of the northern relic: its average fractional polarization is of ∼40 per cent, reaching levels as high as ∼70 per cent. This could be a consequence of the shock passage – the turbulent magnetic field is compressed and its component in the direction of the shock is suppressed.

5.2 Rotation measure synthesis

We applied the RM synthesis technique (Burn 1966; Brentjens et al. 2005) on the linearly polarized data presented in Fig. 11 in order to recover the Faraday depth of the relic.

In addition to the SRT data, for which the frequency band goes from 6.0 up to 7.2 GHz with a channel width ∼1.46 MHz, we also included two more channels taken from the archival VLA data at 4.835 and 4.885 GHz presented in Section 4.3.2. This helped us to improve the reliability of the RM synthesis technique by extending the λ^2 coverage. We smoothed the VLA U and Q images to the SRT resolution. However, the resulting RM transfer function has still a quite large FWHM (∼4000 rad m^{-2}), since we are observing at relatively high frequencies. We should also consider that the angular resolution of our polarized images corresponds to a linear scale of ∼550 kpc, which could be larger than the autocorrelation length of the RM fluctuations. Indeed, it is hard to distinguish multiple components in the Faraday depth space, and as a consequence, we cannot verify if the RM originates internally to the radio relic or in an external Faraday screen. For these reasons, in what follows we assumed that the RM originates entirely in the ICM between us and the relic and that the internal Faraday rotation is negligible. In practice, we considered just one polarized component in Faraday space and we computed its RM from the RM synthesis by measuring the Faraday depth of the polarization peak.

Fig. 11 shows, on the right, the results of the RM synthesis applied on pixels with a polarized S/N ratio larger than 3. The top right panel shows the resulting Faraday depth, while the bottom right panel shows the associated uncertainty.

These errors have been evaluated with a Monte Carlo simulation. We injected 30 different components in Faraday depth, randomly distributed between −10 000 and 10 000 rad m^{-2}, with intensities ranging from 1 up to 4 mJy beam^{-1} to reproduce the S/N range of the observed polarization intensity. From these values, we produced simulated U and Q data in the selected frequency band (SRT C-band plus the two VLA frequencies). We fixed the relic spectral index to what found in Section 4.4 and we assumed a weight w_{ch} for

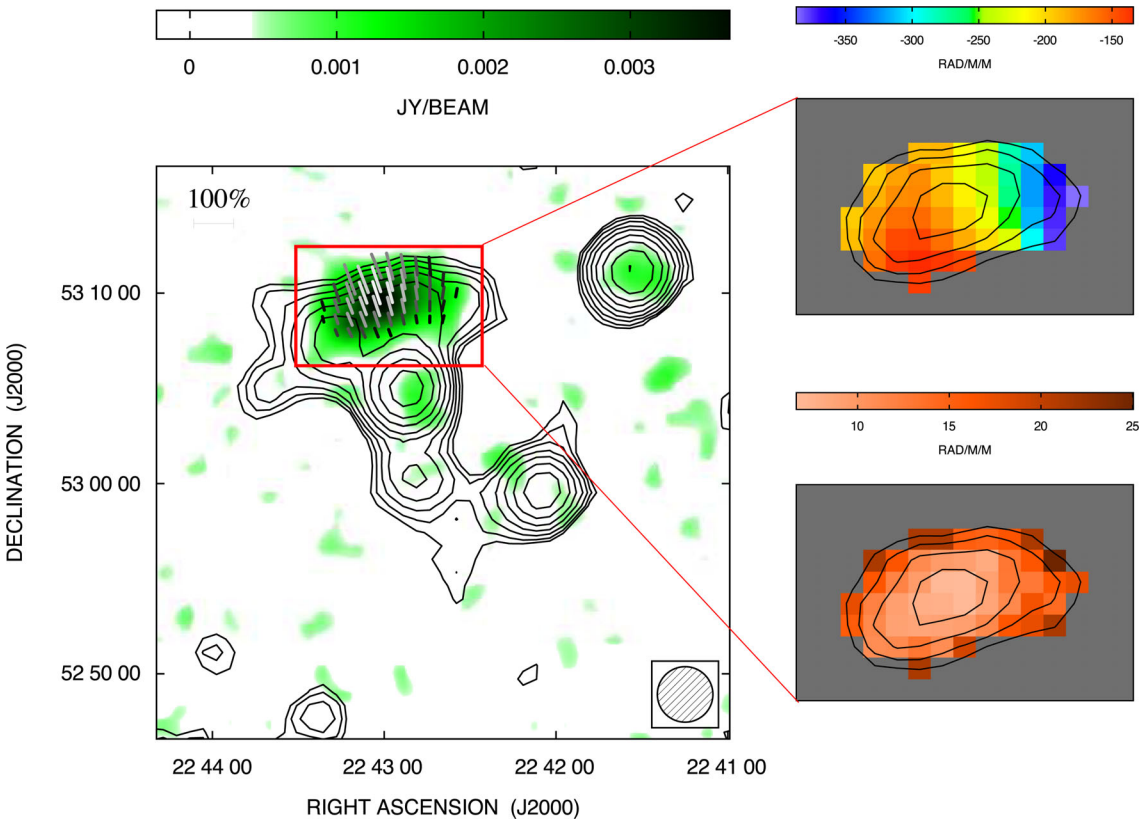

Figure 11. Left: SRT linearly polarized intensity image of the galaxy cluster CIZA J2242.8+5301 obtained from the spectral average in the frequency range 6–7.2 GHz. The FoV of the image is 30 arcmin × 30 arcmin. The FWHM beam is 2.9 arcmin and is shown in bottom right corner. The noise level is 0.35 mJy beam^{-1}. Contours refer to the total intensity image starting at the 3σ level and increasing by factors of $\sqrt{2}$. The vectors indicate the electric-field polarization with the orientation corresponding to the polarization angle and the length proportional to the polarization percentage where 100 per cent is shown in the top left corner. The vectors are traced only for pixels with a total and linearly polarized intensity signal higher than 3σ and an error of the polarization angle below 10°. Right: result of the application of the RM synthesis technique. The top panel on the right represents the Faraday depth we obtained for the maximum polarized signal. In the bottom panel, we report the associated uncertainties evaluated from simulations.

each frequency channel (defined as $w_{ch} = 1/(\sigma_{ch}^2)$ where σ_{ch} is the rms of the single channel), in order to accurately reproduce the effect of the noise on data. We used $w_{ch} = 0$ for those channels that have been blanked due to RFI. We applied the RM synthesis to the simulated U and Q data and we compared the injected values with respect to the polarized signal and the Faraday depth inferred from the RM synthesis. We assumed for the RM uncertainty the rms of the distribution of the difference between input and 'measured' Faraday depth. As expected, the higher the S/N ratio, the lower the rms. For an S/N = 3, the RM uncertainty is about 25 rad m^{-2}, but it decreases down to 7 rad m^{-2} at the position with the brightest polarized emission (S/N = 10).

The Faraday depth image shows negative values with a gradient along the relic length from about -150 at the east end to about -400 rad m^{-2} at the west end. At the polarization peak, we found RM = ($-$ 176 $\pm$ 8) rad m^{-}2. Our Faraday depth image is in good agreement with the values obtained by Kierdorf et al. (2016), but we observe an RM gradient of $\sim$250 rad m^{-2} over an angular scale of 10 arcmin, a factor of 2 larger than the gradient inferred from that work.

We estimated the Galactic RM contribution in the position of CJ2242 using the reconstruction of Oppermann et al. (2015) that provides an $RM_{gal} = (-73 \pm 70)$ rad m^{-2}. Therefore, despite the large uncertainties the Faraday depth shown in Fig. 11 seems to exceed the Galactic contribution by at least a factor of 2. Furthermore one could ask if the observed RM gradient is due to a gradient in the foreground Galactic RM since CJ2242 is very close to the Galactic plane (latitude $b = -5\overset{\circ}{.}11$). Using the map of Oppermann et al. (2015), we deduced that in general RM gradients as large as 1000 rad m^{-2} deg^{-1} are possible along the Galactic plane. In order to explain the RM gradient observed along the northern relic in CJ2242, we would need a very high gradient of about 1500 rad m^{-2} deg^{-1}.

We therefore deduce that the RM gradient is not due to the Galactic foreground. Thus, we can subtract the constant value of $RM_{gal} = -73$ rad m^{-2}, and evaluate if the residual RM could be caused by the magneto-ionic medium in the galaxy cluster itself. Following Govoni et al. (2010), and assuming a cluster magnetic field with an autocorrelation length $\Lambda_B << L$, where L is the integration path along the gas density distribution, the observed RM along a line of sight is a random walk process that involves a large number of cells with size Λ_B. The distribution of the RM will be a Gaussian with zero mean and a variance:

$$\sigma^2_{RM} = < RM^2 > = (812)^2 \Lambda_B \int_0^L (n_e B_\parallel)^2 dl \quad (5)$$

Assuming that the cluster magnetic field follows a η profile with respect to the density distribution $B(r) = B_0(n_e(r)/n_0)^\eta$ and that the density distribution follows a β profile $n(r) = n_0(1 + r^2/r_\perp^2)^{-3\beta/2}$, we obtain that the RM dispersion at a given projected distance $r_\perp$ is:

$$\sigma_{RM}(r_\perp, L) = \frac{K(L) B_0 \Lambda_B^{1/2} n_0 r_c^{1/2}}{\left(1 + \frac{r_\perp^2}{r_c^2}\right)^{\frac{6\beta(1+\eta)-1}{4}}} \sqrt{\frac{\Gamma\left[3\beta(1+\eta) - \frac{1}{2}\right]}{\Gamma[3\beta(1+\eta)]}} \quad (6)$$

where $K(L)$ depends on the integration path along the gas density distribution. We assume that the northern relic is located halfway the cluster so that $K = 441$. B_0 and n_0 are, respectively, the central values of the magnetic field and thermal plasma density profiles, r_c is the core radius of the cluster and Γ is the gamma function. The observed RM image is compatible with a magnetic field tangled on a scale equal or larger than the RM structure of Fig. 11, so that we can assume $\Lambda_B \sim 1300$ kpc. If we subtract from the RM of the peak the Galactic contribution, the residual RM due to the ICM is RM = -103 rad m^{-2}. Assuming reasonable values for the parameters of the hot ICM ($n_0 = 10^{-3}$ cm^{-3}, $\beta = 0.6$ and $r_c = 500$ kpc), we would need a magnetic field of $B_0 = 4.5$ μG at the cluster centre with $\eta = 0.5$ to generate an RM distribution with a $\sigma_{RM} \sim 107$ rad m^{-2} at the relic, where we expect B = 1.6 μG. We note however that even if the central magnetic field strength is in line with what typically found at the centre of galaxy clusters (Feretti et al. 2012), the magnetic field autocorrelation length is much larger than what expected for the turbulent ICM. We also note that the condition $\Lambda_B << L$ could not be verified in our case, since the scale of the magnetic field would be comparable with the size of the cluster.

Another possibility is to consider that the Faraday rotation is occurring in a cosmic web filament which includes CJ2242. As suggested by Planck Collaboration XIX (2016), the primordial magnetic fields have a strength not larger than a few nano Gauss. Even assuming a thermal density of $n_e = 10^{-4}$ cm^{-3} and a magnetic field tangled on a scale of 1300 kpc, the resulting RM would be only $\sim$0.1 rad m^{-2}, making the filament contribution irrelevant. Moreover we notice that magnetic fields of the order of ~ 0.1 μG in filaments should be reached only in the presence of small-scale dynamo amplification in excess of what can be presently resolved by simulation (Vazza et al. 2015). This may be verified in the presence of small-scale vorticity and/or plasma instabilities of various kinds (e.g. Mogavero & Schekochihin 2014), which would however make the magnetic field tangled on much smaller scales than what is inferred by our observations.

For this analysis, it is clear that high-resolution polarized observations are needed to clarify the nature of the observed Faraday rotation in CJ2242. For instance, the forthcoming Westerbork Observations of the Deep APERTIF Northern-Sky (Röttgering et al. 2011) project will give us a polarized image of the northern sky. The high resolution and sensitivity of this survey will make it possible to better investigate the RM observed in the region covered by the galaxy cluster CJ2242 and will help to constrain the properties of the intracluster magnetic field.

6 CONCLUSIONS

We observed the galaxy cluster CIZA J2242.8+5301 with the SRT to further study its diffuse radio emission. We conducted observations in three frequency bands centred at 1.4, 6.6 and 19 GHz. These single-dish data were also combined with archival interferometric observations at 1.4 and 1.7 GHz taken with WSRT.

From the single-dish–interferometer combined images, we measured a flux density of $S_{1.4\,GHz} = (158.3 \pm 9.6)$ mJy for the central radio halo and $S_{1.4\,GHz} = (131 \pm 8)$ and $S_{1.4\,GHz} = (11.7 \pm 0.7)$ mJy for the northern and the southern relics, respectively. At 6.6 GHz, we measured $S_{6.6\,GHz} = (19.3 \pm 1.1)$ mJy for the northern relic and $S_{6.6\,GHz} = (0.9 \pm 0.5)$ mJy for the southern relic. Assuming simple DSA, we interpret the measurements of the northern relic with a CI model, represented by a broken power law. This gave us an injection spectral index $\alpha_{inj} = 0.7 \pm 0.1$ and a spectral index $\alpha = 1.2 \pm 0.1$, resulting in a Mach number M = 3.3 $\pm$ 0.9, consistent with the recent X-ray estimates. No significant steepening of the relic radio emission beyond 2.5 GHz is seen in the data up to 8.35 GHz. By fitting with a simple power-law spectrum ($S_\nu \propto \nu^{-\alpha}$) the measurements of the southern relic, we obtained a spectral index $\alpha = 1.7 \pm 0.7$, corresponding to a Mach number M = 2.0 $\pm$ 0.7, in agreement within the errors with the X-ray estimates. The properties of the

radio halo, namely its largest linear size and radio power, together with the cluster X-ray luminosity, have been compared to those of the other radio haloes known in literature. We found that the radio halo in CJ2242 is the most largest and among the most luminous haloes ever studied.

In the SRT image at 1.4 GHz, we noticed an extended 'L-shaped' emission located about 10 Mpc north-east of CJ2242. The radio emission seems to connect a few spots of X-ray emission. In particular, the X-ray source closest to CJ2242 is associated with the RASS FSC source 1RXS J224504.3+532800, which has a hardness ratio of 0.93 ± 0.09, and with the second RASS Source Catalogue source 2RXS J224454.9+532719 with a hardness ratio of 1.0 ± 0.1. Because of its high hardness ratio, we classify this source as a galaxy cluster candidate. Moreover, at the centre of the X-ray source, we found a head–tail radio galaxy that further supports the presence of a dense medium, typical of a galaxy cluster. The head–tail is associated with the galaxy 2MASX J22445464+5328318 and at less than 0.7 arcmin, we also found the galaxy 2MASX J22445565+5327578. No spectroscopic redshifts are available for these galaxies, however, by using the *K*-band magnitude–redshift relations of Inskip et al. (2002), we estimated a redshift $z \sim 0.1$–0.2 close to that of CJ2242. We obtained a similar result ($z \sim 0.15$–0.2) when considering the *K*-band magnitude–redshift relation for the brightest cluster galaxies (Stott et al. 2008).

With the help of the new SRT measurements at 19 GHz, we studied the spectra of the radio galaxies in CJ2242 with the aim to subtract their contribution to the extended emission of the 6.6 GHz SRT image. In addition, we estimated the synchrotron age of these radio galaxies. We found that most of them are active sources whose radio spectrum is very well reproduced by a CI model. However, one of them we classify as a dying radio galaxy on the basis of the exponential cut-off in the integrated spectrum and on the relaxed morphology. This finding confirms the tendency for these rare radio sources to be preferentially found in the dense environment of galaxy clusters (Murgia et al. 2011). We notice that the dying source is close to an arc-like feature which appears to be a secondary shock or a possible extension of the northern relic, although a discontinuity between these two structures is present. The remnant lobes could be a source of seed electrons for the relic shock wave, a possibility that has already been suggested in case of other galaxy clusters (Bonafede et al. 2014; van Weeren et al. 2017).

Finally, we evaluated the RM of the northern relic by applying the RM synthesis technique at the 6.6 GHz data. The Faraday depth image shows negative values with a gradient along the relic length from about -150 at the east end to about $-400\,\mathrm{rad\,m^{-2}}$ at the west end. At the polarization peak, we found $\mathrm{RM} = (-176 \pm 8)\,\mathrm{rad\,m^{-2}}$. Our Faraday depth image is in good agreement with that obtained by Kierdorf et al. (2016). We derive the presence of an RM gradient of $\sim 250\,\mathrm{rad\,m^{-2}}$ over an angular scale of 10 arcmin, a factor of 2 larger than the gradient inferred in that work. These results provide insights on the magnetic field structure of the ICM surrounding the relic, but further observations are needed to clarify the nature of the observed Faraday rotation.

In conclusion, this study demonstrates that single-dish observations can be helpful to properly study the diffuse emission in galaxy clusters, especially when used in combination with interferometric observation at higher resolution. Future observations at frequencies higher than 10 GHz could be obtained with the new SRT seven-feed *K*-band receiver, and could play a decisive role to constraining the physics of relic sources, and helping to distinguish between the different acceleration models proposed to explain the origin of the relativistic electrons.

ACKNOWLEDGEMENTS

We thank an anonymous referee for her/his comments and suggestions which helped us to improve this paper. The Sardinia Radio Telescope (Bolli et al. 2015; Prandoni et al. 2017) is funded by the Ministry of Education, University and Research, Italian Space Agency, the Autonomous Region of Sardinia (RAS) and the National Institute for Astrophysics (INAF) itself and is operated as National Facility by INAF. The development of the SArdinia Roach2-based Digital Architecture for Radio Astronomy (SARDARA) back end has been funded by the RAS using resources from the Regional Law 7/2007 'Promotion of the scientific research and technological innovation in Sardinia' in the context of the research project CRP-49231 (year 2011, PI: Possenti): 'High resolution sampling of the Universe in the radio band: an unprecedented instrument to understand the fundamental laws of the nature'. FL gratefully acknowledges Sardinia Regional Government for the financial support of her PhD scholarship (P.O.R. Sardegna F.S.E. Operational Programme of the Autonomous Region of Sardinia, European Social Fund 2007–2013 – Axis IV Human Resources, Objective l.3, Line of Activity l.3.1.). This research was partially supported by PRIN-INAF 2014. The NRAO is a facility of the National Science Foundation, operated under cooperative agreement by Associated Universities, Inc. This research made use of the NASA/IPAC Extragalactic Database (NED) which is operated by the Jet Propulsion Laboratory, California Institute of Technology, under contract with the National Aeronautics and Space Administration. Basic research in radio astronomy at the Naval Research Laboratory is funded by 6.1 Base funding. This research was supported by the DFG Forschengruppe 1254 Magnetisation of Interstellar and Intergalactic Media: The Prospects of Low-Frequency Radio Observations. FV acknowledges funding from the European Union's Horizon 2020 research and innovation programme under the Marie-Sklodowska-Curie grant agreement no. 664931. This publication makes use of data products from the Two Micron All Sky Survey, which is a joint project of the University of Massachusetts and the Infrared Processing and Analysis Center/California Institute of Technology, funded by the National Aeronautics and Space Administration and the National Science Foundation. This research used the facilities of the Canadian Astronomy Data Centre operated by the National Research Council of Canada with the support of the Canadian Space Agency.

REFERENCES

Akamatsu H., Kawahara H., 2013, PASJ, 65, 16A
Akamatsu H. et al., 2015, A&A, 582, A87
Basu K., Vazza F., Erler J., Sommer M., 2016, A&A, 591, A142
Boller T., Freyberg M. J., Trümper J., Haberl F., Voges W., Nandra K., 2016, A&A, 588, A103
Bolli P. et al., 2015, J. Astron. Instrum., 4, 1550008-880
Bonafede A. et al., 2009, A&A, 503, 707
Bonafede A., Intema H. T., Brüggen M., Girardi M., Nonino M., Kantharia N., van Weeren R. J., Röttgering H. J. A., 2014, ApJ, 785, 1
Botteon A., Gastaldello F., Brunetti G., Kale R., 2016, MNRAS, 463, 1534
Brentjens M. A., de Bruyn A. G., 2005, A&A, 441, 1217
Burn B. J., 1966, MNRAS, 133, 67
Carilli C. L., Taylor G. B., 2002, ARA&A, 40, 319
Carilli C. L., Perley R. A., Dreher J. W., Leahy J. P., 1991, ApJ, 383, 554
Carretti E. et al., 2013, MNRAS, 430, 1414
Condon J. J., Cotton W. D., Greisen E. W., Yin Q. F., Perley R. A., Taylor G. B., Broderick J. J., 1998, AJ, 115, 1693
Dasadia S. et al., 2016, ApJ, 820, L20
Dawson W. A. et al., 2015, ApJ, 805, 143

Donnert J. M. F., Beck A. M., Dolag K., Röttgering H. J. A., 2017, MNRAS, 471, 4587
Donnert J. M. F., Stroe A., Brunetti G., Hoang D., Roettgering H., 2016, MNRAS, 462, 2014
Drury L. O., 1983, Rep. Prog. Phys., 46, 973
Ebeling H., Mullis C. R., Tully R. B., 2002, ApJ, 580, 774
Ebeling H. et al., 2013, MNRAS, 432, 62
Emerson D., 2002, in Stanimirovic S., Altschuler D., Goldsmith P., Salter C. eds, ASP Conf. Ser. Vol. 278, Single-dish radio astronomy: techniques and applications. Astron. Soc. Pac., San Francisco, p. 27
Ensslin T. A., Biermann P. L., Klein U., Kohle S., 1998, A&A, 332, 395
Farnsworth D., Rudnick L., Brown S., Brunetti G., 2013, ApJ, 779, 189
Feretti L., Giovannini G., Govoni F., Murgia M., 2012, A&AR, 20, 54
Giovannini G., Vacca V., Girardi M., Feretti L., Govoni F., Murgia M., 2013, MNRAS, 435, 518
Girardi M. et al., 2016, MNRAS, 456, 2829
Govoni F., Murgia M., Feretti L., Giovannini G., Dallacasa D., Taylor G. B., 2005, A&A, 430, L5
Govoni F. et al., 2010, A&A, 522, A105
Govoni F., Ferrari C., Feretti L., Vacca V., Murgia M., Giovannini G., Perley R., Benoist C., 2012, A&A, 545, A74
Govoni F. et al., 2017, A&A, 603, A122
Hoang D. N. et al., 2017, MNRAS, 471, 1107
Inskip K. J., Best P. N., Longair M. S., MacKay D. J. C., 2002, MNRAS, 329, 277
Intema H. T., Jagannathan P., Mooley K. P., Frail D. A., 2017, A&A, 598, A78
Kang H., Ryu D., 2016, ApJ, 823, 13
Kardashev N. S., 1962, SvA, 6, 317
Kierdorf M., Beck R., Hoeft M., Klein U., van Weeren R. J., Forman W. R., Jones C., 2017, A&A, 600, A18
Killeen N. E. B., Bicknell G. V., Ekers R. D., 1986, ApJ, 302, 306
Kocevski D. D., Ebeling H., Mullis C. R., Tully R. B., 2007, ApJ, 662, 224
Martinez Aviles G. et al., 2016, A&A, 595, A116
Mogavero F., Schekochihin A. A., 2014, MNRAS, 440, 3226
Murgia M., Fanti C., Fanti R., Gregorini L., Klein U., Mack K.-H., Vigotti M., 1999, A&A, 345, 769
Murgia M. et al., 2011, A&A, 526, A148
Murgia M., Markevitch M., Govoni F., Parma P., Fanti R., de Ruiter H. R., Mack K.-H., 2012, A&A, 548, A75
Murgia M. et al., 2016, MNRAS, 461, 3516
Ogrean G. A., Brüggen M., Röttgering H., Simionescu A., Croston J. H., van Weeren R., Hoeft M., 2013, MNRAS, 429, 2617
Ogrean G. A., Brüggen M., van Weeren R., Röttgering H., Simionescu A., Hoeft M., Croston J. H., 2014, MNRAS, 440, 3416
Okabe N., Akamatsu H., Kakuwa J., Fujita Y., Zhang Y., Tanaka M., Umetsu K., 2015, PASJ, 67, 114
Oppermann N. et al., 2015, A&A, 575, A118
Pacholczyk A. G., 1970, Series of Books in Astronomy and Astrophysics. Freeman, San Francisco
Parekh V., Dwarakanath K. S., Kale R., Intema H., 2017, MNRAS, 464, 2752
Perley R. A., Butler B. J., 2013, ApJS, 204, 19
Planck Collaboration IV, 2013, A&A, 550, A130
Planck Collaboration XIX, 2016, A&A, 594, A19
Prandoni I. et al., 2017, preprint (arXiv:1703.09673)
Rengelink R. B., Tang Y., de Bruyn A. G., Miley G. K., Bremer M. N., Roettgering H. J. A., Bremer M. A. R., 1997, A&AS, 124, 259
Röttgering H. et al., 2011, J. Astrophys. Astron., 32, 557
Röttiger K., Burns J. O., Stone J. M., 1999, ApJ, 518, 603
Sarazin C. L., 2002, in Feretti L., Gioia I.M., Giovannini G., eds, Astrophysics and Space Science Library, Vol. 272, Merging Processes in Galaxy Clusters. Kluwer Academic Publishers, Dordrecht, p. 1
Sault R. J., Teuben P. J., Wright M. C. H., 1995, in Shaw R.A., Payne H.E., Hayes J.J.E., eds, ASP Conf. Ser. Vol. 77, Astronomical Data Analysis Software and Systems IV. Astron. Soc. Pac., San Francisco, p. 433
Schlafly E. F., Finkbeiner D. P., 2011, ApJ, 737, 103
Shakouri S., Johnston-Hollitt M., Pratt G. W., 2016, MNRAS, 459, 2525
Stanimirovic S., Staveley-Smith L., Dickey J. M., Sault R. J., Snowden S. L., 1999, MNRAS, 302, 417
Stott J. P., Edge A. C., Smith G. P., Swinbank A. M., Ebeling H., 2008, MNRAS, 384, 1502
Stroe A., van Weeren R. J., Intema H. T., Röttgering H. J. A., Brüggen M., Hoeft M., 2013, A&A, 555, A110
Stroe A., Harwood J. J., Hardcastle M. J., Röttgering H. J. A., 2014, MNRAS, 445, 1213
Stroe A. et al., 2016, MNRAS, 455, 2402
Trasatti M., Akamatsu H., Lovisari L., Klein U., Bonafede A., Brüggen M., Dallacasa D., Clarke T., 2015, A&A, 575, A45
Truemper J., 1993, Science, 260, 1769
van Weeren R. J., Röttgering H. J. A., Brüggen M., Hoeft M., 2010, Science, 330, 347
van Weeren R. J., Brüggen M., Röttgering H. J. A., Hoeft M., 2011, MNRAS, 418, 230
van Weeren R. J., Bonafede A., Ebeling H., Edge A. C., Brüggen M., Giovannini G., Hoeft M., Röttgering H. J. A., 2012, MNRAS, 425, L36
van Weeren R. J. et al., 2017, Nat. Astron., 1, 0005
Vazza F., Ferrari C., Brüggen M., Bonafede A., Gheller C., Wang P., 2015, A&A, 580, A119
Voges W. et al., 1999, A&A, 349, 389

[1]*INAF – Osservatorio Astronomico di Cagliari, Via della Scienza 5, I-09047 Selargius (CA), Italy*
[2]*Dipartimento di Fisica, University of Cagliari, Strada Prov.le Monserrato-Sestu Km 0.700, I-09042 Monserrato (CA), Italy*
[3]*INAF – Istituto di Radioastronomia, Via Gobetti 101, I-40129 Bologna, Italy*
[4]*Dipartimento di Fisica e Astronomia, Università degli Studi Bologna, Viale Berti Pichat 6/2, I-40127 Bologna, Italy*
[5]*INAF – IASF Milano, Via Bassini 15, I-20133 Milano, Italy*
[6]*Dipartimento di Fisica dell'Università degli Studi di Trieste – Sezione di Astronomia, via Tiepolo 11, I-34143 Trieste, Italy*
[7]*INAF – Osservatorio Astronomico di Trieste, via Tiepolo 11, I-34143 Trieste, Italy*
[8]*Hamburger Sternwarte, Universität Hamburg, Gojenbergsweg 112, D-21029 Hamburg, Germany*
[9]*Agenzia Spaziale Italiana (ASI), via del Politecnico snc I-00133 Rome, Italy*
[10]*Fundación G. Galilei – INAF TNG, Rambla J. A. Fernández Pérez 7, E-38712 Breña Baja (La Palma), Spain*
[11]*Instituto de Astrofísica de Canarias, C/Vía Láctea s/n, E-38205 La Laguna (Tenerife), Spain*
[12]*Departamento de Astrofísica, Univ. de La Laguna, Av. del Astrofísico Francisco Sánchez s/n, E-38205 La Laguna (Tenerife), Spain*
[13]*Naval Research Laboratory, Washington, DC 20375, USA*
[14]*School of Physics, University of the Witwatersrand, Private Bag 3, 2050, Johannesburg, South Africa*
[15]*Max Planck Institut für Astrophysik, Karl-Schwarzschild-Str.1, D-85740 Garching, Germany*
[16]*Laboratoire Lagrange, UCA, OCA, CNRS, Blvd de l'Observatoire, CS 34229, F-06304 Nice Cedex 4, France*
[17]*University of Leiden, Rapenburg 70, NL-2311 EZ Leiden, the Netherlands*
[18]*Peripety Scientific Ltd., PO Box 11355 Manners Street, Wellington 6142, New Zealand*
[19]*School of Chemical & Physical Sciences, Victoria University of Wellington, PO Box 600, Wellington 6140, New Zealand*
[20]*Argelander-Institut für Astronomie, Auf dem Hügel 71 D-53121 Bonn, Germany*
[21]*ASTRON, the Netherlands Institute for Radio Astronomy, Postbus 2, NL-7990 AA, Dwingeloo, The Netherlands*
[22]*National Radio Astronomy Observatory, PO Box O, Socorro, NM 87801, USA*
[23]*Department of Physics and Astronomy, University of New Mexico, Albuquerque, NM 87131, USA*

This paper has been typeset from a TEX/LATEX file prepared by the author.